CHALMERS
UNIVERSITY OF TECHNOLOGY

An ultrasonic MEMS-based airspeed sensor for lightweight drones

Master's thesis in Embedded Electronic System Design

Martin Bengts

Department of Microtechnology and Nanoscience
CHALMERS UNIVERSITY OF TECHNOLOGY
Gothenburg, Sweden 2026

Master's thesis 2026

An ultrasonic MEMS-based airspeed sensor for lightweight drones

MARTIN BENGTS

Department of Microtechnology and Nanoscience
Chalmers University of Technology
Gothenburg, Sweden 2026

An ultrasonic MEMS-based airspeed sensor for lightweight drones
Martin Bengts

Supervisor: Lars Svensson, Department of Microtechnology and Nanoscience
Company advisor: Fredrik Falkman, Sjöräddningssällskapet
Examiner: Per Larsson-Edefors, Department of Microtechnology and Nanoscience

Master's Thesis 2026
Department of Microtechnology and Nanoscience
Chalmers University of Technology
SE-412 96 Gothenburg
Telephone +46 31 772 1000

Typeset in LaTeX
Gothenburg, Sweden 2026

An ultrasonic MEMS-based airspeed sensor for lightweight drones
Martin Bengts
Department of Microtechnology and Nanoscience
Chalmers University of Technology

Abstract

This thesis is conducted together with the Swedish Sea Rescue Society (SSRS), where an ultrasonic airspeed sensor for lightweight fixed-wing drones is developed. The project acts as an alternative to the currently used sensor on the drone, which is based on a Pitot-static system. The ultrasonic technique has shown significant potential for airspeed measurement. This work further explores the technique with the aim of developing a compact sensor design better suited for small aerial vehicles. To achieve this, ultrasonic Micro Electro Mechanical Systems (MEMS) are utilized.

The developed prototype consists of three main parts. First, two transceiver modules which are facing each other at a 45° angle relative to the airflow, enabling collection of upwind and downwind data. Second, a microcontroller software that controls the transceivers and produces airspeed estimations. Third, a control circuit which enables communication between microcontroller software and transceiver modules. The core of the airspeed estimation is based on the difference between upwind and downwind data, along with different signal processing techniques.

The results demonstrate that the prototype offers advantages in terms of size, weight and power consumption, with the potential to match conventional Pitot-static systems. Furthermore, the developed prototype is able to accurately record airspeed in one direction. It also demonstrates the limitations of this kind of hardware, as well as the ultrasonic airspeed measurement technique in general.

Keywords: Pitot-static system, Micro Electro Mechanical Systems, ultrasonic transceiver module, airspeed estimations, microcontroller software

Acknowledgements

First, I would like to thank the Swedish Sea Rescue Society (SSRS) for allowing me to do the thesis with them. A special thanks to my organization supervisor Fredrik Falkman, which helped me understand the purpose and the expected outcome of the project.

I am thankful for the opportunity to utilize the lab facilities at Chalmers. I want to acknowledge the CASE Lab that provided me with the components and tools needed. I also want to acknowledge Chalmers Laboratory of Fluids and Thermal Sciences for providing the wind tunnel and measurement equipment. These resources have been invaluable to be able to build and evaluate the developed prototype.

Furthermore, I would also like to say a big thank you to my academic supervisor Lars Svensson for his guidance, support and encouragement throughout the complete project.

Lastly, I would like to thank my examiner Per Larsson-Ederfors for his guidance and feedback in writing a well structured report.

Martin Bengts, Gothenburg, June 2026

Contents

1 Introduction

Airspeed is the speed of an object that is relative to the air mass it is flying through. Measured airspeed is fundamental for safe operations of aerial vehicles [1]. Among other reasons, measured airspeed is essential to avoid losing control over the vehicle in low speed (stall condition), and to not reach the limitations of the vehicle's mechanical structure during high speeds. Using conventional aircraft terminology, indicated airspeed is the term used for the direct reading from the airspeed measurement instrument. This airspeed can then be compensated for in terms of e.g. temperature, static position error and pressure deviations to obtain the true airspeed of the vehicle. Traditionally, indicated airspeed is extracted using various pressure measurement methods, such as Pitot-static tubes.

This project is developed in collaboration with the Swedish Sea Rescue Society (SSRS), a voluntary sea rescue organization that patrols the Swedish coastline [2]. The organization is developing a new type of lightweight fixed wing drone that will be stationed along the coast to provide rescue personnel with critical information before they arrive on scene.

The drone requires several types of sensors to collect information about the environment, in order to help the autopilot control the vehicle more efficiently. One of those sensors is the airspeed sensor, which currently is based on a Pitot-static system. However, the drone is expected to operate in harsh weather conditions where such systems can experience significant problems, experience icing or be clogged by raindrops.

This has led to a project that investigates the feasibility of the ultrasonic technology in airspeed measurement. Ultrasonic measurement techniques are well established in applications involving liquid flow measurements and wind measurements, also called anemometry. The fundamentals of those techniques should also be possible to use within airspeed measurement, since measured airflow will be the same. It is only the reference frame that changes. So, if a wind measurement device is placed on a moving object, it will measure the speed relative to the object, and not the ground as it is during wind measurements, but the fundamental idea will be the same. Previous phases of the project [3, 4] have been carried out using more traditional ultrasonic elements, demonstrating the possibilities and potentials of this method. However, further development and refinements are required before the technology can satisfy the requirements needed for small aerial vehicles. This time, SSRS want the project to explore the possibilities for a smaller sensor design that can actually fit these types of applications.

Recently, there have been advancements in ultrasonic Micro Electro Mechanical Systems (MEMS) technology, where sensing elements and signal processing are integrated on a single chip. This offers an attractive path for developing a more compact and integrated solution for ultrasonic airspeed measurement [5]. This technology can contribute to lower power consumption and improved design, more suited for a small aerial vehicle. This version of the project investigates the feasibility of these kinds of ultrasonic MEMS in airspeed measurements.

1.1 Related Work

Ultrasonic anemometry has been around and used for a long time in meteorology, where ultrasonic anemometers provide high speed measurements and good precisions by comparing upstream and downstream time-of-flight (ToF) [6]. These anemometers demonstrate that ultrasonic sensors can accurately extract airflow velocity. However, traditional ultrasonic anemometers rely on relatively large mechanical frames, which is a significant disadvantage for small scale aerial vehicles.

Two prototypes are presented in [3] and [4]. One of them utilizes the Doppler beam swinging technique and presents a promising result, where it is capable of measuring airspeed between 0 m/s and 17 m/s, with a limitation of the maximum frequency in the ultrasonic elements. However, the report does not present the accuracy and precision of the measurements, which makes the results uncertain. The other prototype is based on the ToF technique, featuring two ultrasonic transceivers pointed towards each other. This prototype also shows promising results with acceptable precision up to 10 m/s. However, to obtain more accurate measurements, more calibration and work would be needed, especially for higher airspeeds.

Measuring airspeed with ultrasonic MEMS has been successfully tested with good precision for low speeds at indoor environments, as presented in [7]. In that project, an ultrasonic sensor called CH101 is used, which is a low cost and power efficient ToF ultrasonic MEMS [8]. The sensor has a piezoelectric micromachined ultrasonic transceiver (PMUT), and a system on chip (SoC), which produces ready to use distance data. The study suggests several algorithms that can be performed with these types of sensors to extract airspeed information. In [7] the ToF data is extracted and the phase information from it is utilized to perform airspeed calculations. However, the study also discusses the limitations of only focusing on phase information, which limits the airspeed range. Some of the suggested algorithms aim to work around that problem, which indicates that more information than just phase data is needed to be utilized for measurements of higher airspeeds, with acceptable precision.

1.2 Purpose and Goal

Ultrasonic MEMS with SoC has been proven to be feasible for low airspeed applications. Here a higher airspeed case will be investigated for lightweight fixed wing drones. Demonstration of the feasibility of this technology may contribute to an efficient sensor with a minimized design that is more suitable for small aerial vehicles.

The main goal of this project is to develop a sensor prototype that is able to measure airspeeds up to 25 m/s, with a maximum error margin of ±3 m/s, and a minimum output rate of 20 Hz. The aim is also to reach similar numbers in power demand, weight and cost compared to the sensor currently used on the drone (DLVR-L10D) [9]. Furthermore, the developed prototype will also be evaluated in terms of drone compatibility compared to the earlier developed prototypes.

The study will address several challenges, including careful evaluation of sensors, possible electrical control circuits and physical setups that can maximize the signal to noise ratio. Furthermore, the project will demand extensive signal and data processing, including filtering and algorithms to extract accurate airspeed information.

1.3 Limitations

This section presents factors that are considered outside of the project scope.

1.3.1 Transmission Medium

To evaluate the main goals of this project, a wind-tunnel will be used since it will offer a controlled environment with controlled airspeed. However, there are other factors that can influence the speed of sound, such as temperature change, humidity and other particles, for example dust.

These factors will not be taken into consideration to a large extent, as the sensors will be tested in room temperature with small variations, and the composition of humidity and other particles in the air will be considered low. The reason for this is the difficulty in creating these conditions in a controlled testing environment. Which parameters that are affecting the measurement errors the most during actual flights are also not known, which is something that has to be further explored in the case of drone integration. The scope of this project is therefore to measure indicated airspeed, which may require corrections to obtain the vehicle's true airspeed.

Alternatively, to test the system stability, outdoor testing with influences of these factors could be an interesting method, but will not contribute to the more exact evaluation of accuracy and precision.

1.3.2 No Drone Integration

During the thesis work, the ultrasonic airspeed sensor is not planned to be integrated on the drone. Therefore, the thesis will not be able to evaluate the following:

- Sensor-performance during flight, including harsh environments and effects caused by the drone itself, such as vibrations and electromagnetic interference.
- Aerodynamic impact of the sensor module on the drone. However, this will be considered during the development of the physical design.

- How the sensor will impact the battery life of the drone during operation. The power usage for the sensor as a stand-alone unit will be evaluated, which can give indication on how it will work in operation.
- That the sensor system is fully able to communicate with the autopilot system. It will still be taken into consideration during the development to facilitate this in the future.

The drone will, however, be taken into account for all the design decisions during the project. If something is considered as a major risk that would make sensor integration difficult on the drone, it will not be implemented.

1.3.3 Type of Measurements

The Doppler effect is an interesting method of measuring airspeed with ultrasonic technology, especially by measuring the Doppler effect with particles in the air itself as the reflector, which is to some extent done in [3]. This would only need one or more transceivers pointing out in the air, which could contribute to a significant reduction in the required space for the transceiver module. However, the results of the project in [3] are uncertain. That project also used more powerful ultrasonic elements compared to MEMS, and because the Doppler effect relies on how powerful the reflected signal is, ultrasonic MEMS is not going to be a suitable transceiver type for this method.

The Doppler effect can still be an interesting factor to investigate when using static objects as reflectors, or using transceivers in pitch and catch configuration, where the transceivers are facing each other, as further discussed in Section 2.4.

1.4 Thesis Outline

This report provides a thorough process description of the development of an ultrasonic airspeed sensor prototype for fixed-wing light weight drones, using MEMS transceiver modules. Chapter 2 provides the technical principles and concepts needed to understand the progression of this project. Chapter 3 delves into the methods and the tools used to develop the prototype. Chapter 4 presents a detailed design description of the complete sensor module, while also discussing key design decisions. Chapter 5 demonstrates the results of the design and evaluates the ability of the sensor module to accurately measure airspeed. The chapter also provides supplementary measurements and estimation data needed for the overall evaluation of the module. Chapter 6 discusses the interpretation of the results, evaluates whether the project goals have been achieved, and proposes suggestions on how to improve for future work. Chapter 7 offers a conclusion of the report and the project.

2

Technical Background

This chapter describes the technical principles and concepts needed for a reader to understand the progression of this project.

2.1 Pitot Static System

In traditional airspeed measurement for aerial vehicles, indicated airspeed is the term of the direct reading from the airspeed measurement instrument. This provides the airspeed information uncorrected for temperature, static position error and pressure deviations that are required to reach the true airspeed of the vehicle.

Two types of pressures are needed to extract indicated airspeed for aerial vehicles: Total pressure and static pressure [1]. It is common to measure these pressures all at once with a sensor/system called Pitot-static tube. These kinds of systems have one port connected to a Pitot tube, pointed out in the front of the vehicle where it has free airflow, measuring the total pressure. It also has tubes or vents placed in a position where the airspeed is not affecting the pressure, measuring the static pressure.

The information of the total pressure (p_t) and the static pressure p are then used to calculate impact pressure (q_c) as in Equation 2.1 [1].

$$q_c = p_t - p \tag{2.1}$$

The impact pressure then has to be compensated for the air compression in the tube in order to obtain the dynamic pressure (q). This is the parameter that is needed to calculate speed of the body relative to the air (V) with Equation 2.2, where ρ is the air density. However, for lower airspeeds, below 100 m/s, the air can be approximated to be incompressible, which means that the impact pressure is equal to the dynamic pressure and the airspeed can be calculated without air compression compensation.

$$q = \frac{1}{2}\rho V^2 \tag{2.2}$$

2.2 Piezoelectric Ultrasonic Transceivers

A piezoelectric ultrasonic transceiver is a module that is able to transmit and receive sound that has a frequency above 20 kHz. It is made of piezoelectric material that is able to convert an electrical signal into mechanical vibrations (ultrasonic sound) and vice versa.

The most common applications for these kinds of transceivers are to perform non-contact distance measurements by the so called pulse-echo method [10]. This method can be performed mono-statically, which is when one sensor first transmits and then receives its own signal. The distance can be determined by measuring the time (t) it takes between the transmitted signal and the received echo from an object. If the speed of sound (C) is known, the distance to the object (X) can be determined by Equation 2.3. The speed of sound varies depending on temperature and the medium it is traveling through. However, it can be considered as about 343 m/s in dry air at room temperature. Other typical applications that the pulse-echo method enables are presence detection, object shape determination, material investigation and orientation. If instead the distance is known, information about temperature or the transmission medium can be extracted.

$$X = \frac{tC}{2} \tag{2.3}$$

The problem with mono-static operation is a phenomenon called ringing decay, which is the time it takes for the ultrasonic element to end the transmission and ring out until it is ready to start receive its own signal [10]. This is problematic for short distance measurements because it can not distinguish between transmission and echo, which is limiting the minimum distance. This problem could be solved by working with a bi-static approach, which instead utilizes two transceivers in a so called pitch and catch configuration, where the transceivers are facing each other, as shown in Figure 2.1. Measurements are then performed with one transceiver acting as the transmitter and the other as the receiver. The method adds calibration and synchronization requirements, but avoids the need of waiting on the ringing-decay. This kind of operation also enables other areas of use, such as anemometry and flow measurement.

2.3 Sound Propagation in Air

The theoretical expressions for the speed of sound C propagating in air are usually calculated under the assumption that the air behaves as an ideal gas [11]. This expression is presented in Equation 2.4, where P is the ambient pressure, ρ represents the gas density and γ represents the ratio of the specific heat of gas at constant pressure to that constant volume.

$$C = \sqrt{\frac{\gamma P}{\rho}} \tag{2.4}$$

By then substituting P with the ideal gas law, the expression can be rewritten as in Equation 2.5, where R is the universal gas constant, M the molar mass of the gas, and T the absolute temperature in Kelvin.

$$C = \sqrt{\frac{\gamma RT}{M}} \tag{2.5}$$

Because γ and R can be considered as constant (as long as M remains approximately constant), it is clear which external parameters that actually are able to affect the speed of sound. It is mainly the humidity in the air that affects the molar mass M. The humidity can also affect γ which makes it complex to take into consideration in the calculations. However, the humidity can often be neglected as its impact is minimal in comparison to the temperature [10]. This is why the speed of sound often is approximated as in Equation 2.6, where t is the temperature in Celsius and the speed of sound in dry air at 0 °C/273 K is 331 m/s

$$C = 331\sqrt{\frac{T}{273}} \approx 331 + 0.6t \tag{2.6}$$

2.4 Fundamentals in Ultrasonic Anemometry

The most proven way to utilize the ultrasonic technology for airspeed measurement in one direction is within ultrasonic anemometry. This method uses two transceivers that are able to both transmit and receive ultrasonic signals. As shown in Figure 2.1, the transceivers are placed in a so-called pitch and catch configuration where a comparison of upwind and downwind data can be done.

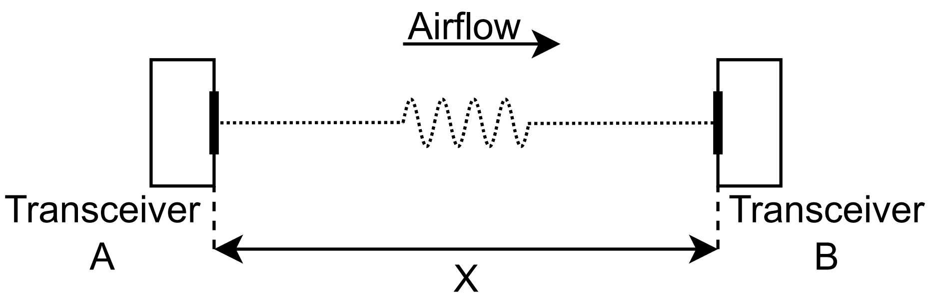

Figure 2.1: Fundamental setup in 1D ultrasonic anemometry.

The method uses the time it takes for the sound waves to travel between the two transceivers [12]. Utilizing the basic relationship between time and length, where time is equal to length divided by speed, Equation 2.7 and 2.8 can then be derived. The time from A to B is denoted by t_{A-B}, and from B to A it is denoted by t_{B-A}.

C is the speed of sound, V is air velocity and X is the static distance between the two transceivers.

$$t_{A-B} = \frac{X}{C+V} \tag{2.7}$$

$$t_{B-A} = \frac{X}{C-V} \tag{2.8}$$

There are then two common formulations for obtaining the airspeed from these two equations. The first uses an approximation where V^2 is assumed to be much less than C^2 and is therefore neglected when subtracting Equation 2.7 from Equation 2.8 [12] which gives the airspeed as in Equation 2.9. This formulation is often chosen when the airspeed is expected to be fairly low, which yields a simpler (linear) relationship between the airspeed and the time difference.

$$V = \frac{\Delta t C^2}{2X} \tag{2.9}$$

The second formulation first rearranges the equations of the basic relationship as seen in Equation 2.10 and Equation 2.11 [13, 12].

$$C + V = \frac{X}{t_{A-B}} \tag{2.10}$$

$$C - V = \frac{X}{t_{B-A}} \tag{2.11}$$

Equation 2.10 is then subtracted from Equation 2.11 which yields Equation 2.12

$$2V = \frac{X}{t_{A-B}} - \frac{X}{t_{B-A}} \tag{2.12}$$

So the airspeed can instead be derived as in Equation 2.13

$$V = \frac{X}{2}\left(\frac{1}{t_{A-B}} - \frac{1}{t_{B-A}}\right) \tag{2.13}$$

This formulation avoids the use of the critical parameter C, which is dependent on external circumstances as for example temperature and humidity. This makes it more suitable when the conditions are varying. However, it yields a more complex relationship between the airspeed and the measured upwind and downwind transit times.

There are different ways to determine upwind and downwind transit time. The most obvious way is by measuring the actual time it takes for the ultrasonic signal to travel between transmitter and receiver. This method theoretically offers a large airspeed range. However, the precision of this method is limited to the sampling rate in the receiver. The study presented in [12] uses a sample rate as high as 2 MSa/s with this kind of method, and is only able to extract an ideal resolution of 0.7588 m/s. This is why systems with lower sample rates often need to utilize other methods to achieve better resolution.

For the first formulation it is also possible to utilize the phase difference between downwind and upwind measurements to obtain the same kind of information as the actual time difference method [14]. This method uses the same sampling point for both cases and provided that both transceivers have synchronized phase, the difference between those will tell the time difference between the directions. Figure 2.2 presents the idea of this method, where the dotted black wave is the received signal at an airspeed of 0 m/s for both upwind and downwind measurement. The dotted blue wave in Figure 2.2a is the downwind signal at a certain airspeed and the dotted green wave in Figure 2.2b is the upwind signal at the same airspeed. The vertical dotted gray lines illustrates the sampling points of the receiver and the phase difference $\Delta\phi$ can be obtained by taking the difference in phase between the blue and green waves at a specific sampling point.

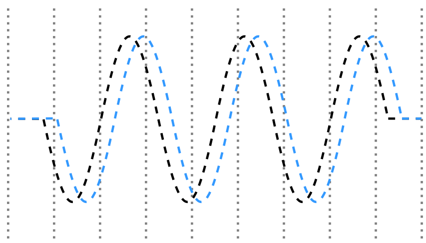

(a) Downwind measurement.

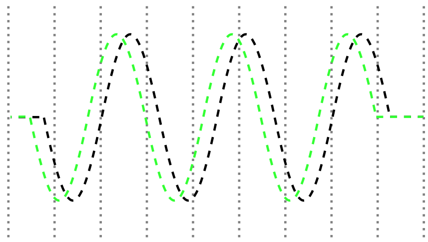

(b) Upwind measurement.

Figure 2.2: Illustration of the phase shift due to applied airspeed.

Δt can then be replaced by $\Delta\phi$ with Equation 2.14, where f_o is the frequency of the transmitted ultrasonic wave.

$$\Delta t = \frac{\Delta\phi}{2\pi f_o} \tag{2.14}$$

The same equations can then be used to determine airspeed V by using Equation 2.14 in Equation 2.9 which yields Equation 2.15

$$V = \frac{\Delta\phi C^2}{4X\pi f_o} \tag{2.15}$$

This method avoids the need of a high sampling rate because it removes the need to know the absolute transit time. The importance for this method is instead that the two transceivers are well synchronized, which means that phase samples in the two transceivers are performed with high precision in time in relation to the transmissions of the ultrasonic waves. This is often possible to do at a higher precision than what is possible by measuring the actual time differences. However, without extra algorithms, this method is limited to a measured phase difference of $\pm\pi$ rad or $\pm 180°$ (which limits the airspeed range).

The phase method cannot be used for the second formulation, as the absolute transit time cannot be eliminated in the same way.

2.5 MEMS Technology

Micro-electromechanical systems are micro actuators and sensors which combine electrical and mechanical functionality on a micrometer scale.

Due to the wide range of use cases MEMS incorporates components with a variety of fabrication methods [15]. Despite the variety, the components are typically created on silicon wafers. Thus the mechanical parts can be integrated with the electronic circuit using the same kind of techniques used for conventional integrated circuits. Therefore systems can be fabricated with both sensing and signal processing on a just a few micrometers.

2.6 Extend Airspeed Measurement Range

As discussed in Section 2.4, the more precise phase difference method in ultrasonic anemometry faces limitations in its measurement range, where it is only able to measure a phase difference of $\pm\pi$ rad or ± 180 degrees. The literature proposes a few ways to overcome the limitation and this section will present what parameters that can be used and some of the proposed algorithms that can be performed.

2.6.1 Magnitude Guidance

The transmitted ultrasonic signal often varies in magnitude during its progression, especially in the beginning and end of the signal. If an appropriate sample is selected to be observed, information of shift between phase cycles could possibly be obtained. The study in [7] presents an algorithm that uses this approach. The algorithm calculates the derivative of the signal magnitude at 0 m/s. By analyzing whether the magnitude has increased or decreased to a certain level, the system can then determine which phase cycle it is currently in.

2.6.2 Real-Time Phase Tracking

Instead of just statically check the phase at each measurement, it could be tracked continuous by introducing memory, where previous measurements is used to obtain the evolution of the phase over time. This method can then track when the phase is doing large jumps, which indicates that the phase has wrapped (exceeded the $\pm\pi$ rad limit). The most basic way to utilize this method is discussed in [16], where the phase value is based on the difference between the current and the previous phase measurement.

$$\tilde{\phi}_i = \tilde{\phi}_{(i-1)} + \Delta\tilde{\phi} \tag{2.16}$$

$$\Delta\tilde{\phi} = \begin{cases} \phi_i - \phi_{(i-1)} - 2\pi, & \phi_i - \phi_{(i-1)} > \pi \\ \phi_i - \phi_{(i-1)} + 2\pi, & \phi_i - \phi_{(i-1)} < -\pi \\ \phi_i - \phi_{(i-1)}, & \text{otherwise} \end{cases} \tag{2.17}$$

Equation 2.16 describes how the current tracked phase value $\tilde{\phi}_i$ is calculated, where $\tilde{\phi}_{(i-1)}$ is the previously calculated phase value. $\Delta\tilde{\phi}$ is obtained by Equation 2.17 and calculates the difference between two phase measurements. If the phase difference is larger than $\pm\pi$ rad it will adapt the value so it follows the phase wrapping from π to $-\pi$ and vise versa. However, this procedure assumes that the actual phase difference between measurements does not exceed π rad, otherwise it would lose track of the rotation direction [7].

2.7 Doppler Effect

If the transmitter and receiver of a wave move relative to each other, the received signal will have a frequency (f_r), shifted compared to the frequency of the transmitted wave (f_t) [17]. This phenomenon is called the Doppler effect and if the receiver is assumed to be static and the source speed u_s is much less than the wave speed (c), this can be described by Equation 2.18.

$$f_r = \frac{c}{c \pm u} f_t \tag{2.18}$$

If the transmitter moves towards the receiver, f_r will be larger than f_t and if it instead moves away, f_r will be lower than f_t.

2.8 Digital Filtering

Digital filters process discrete time signals by sampled continuous time signals. Digital filtering is an important part of Digital Signal Processing (DSP) and whereas analog filters have advantages in responsiveness dynamic range and bandwidth, digital filters are often advantageous in terms of complexity and precision [18]. Digital filters are often separated in two different types: Finite Impulse Response (FIR) filters, by convolution and Infinite Impulse Response (IIR) filters, by recursion.

The traditional implementation of FIR filters are non-recursive filters where the output is based on current and previous input values, which can be expressed by Equation 2.19 [19]. $y[n]$ denotes the output signal, $x[n]$ denotes the input signal, b_i denotes the filter coefficient at tap i and N denotes the order of the filter.

$$y[n] = \sum_{i=0}^{N} b_i x[n-i] \tag{2.19}$$

The output only depends on a limited number of inputs, which enables stability, exact linear phase and is conceptually often more simple to implement although it often require a higher computational cost compared to IIR filters.

The IIR filters calculates the output based on current and previous inputs as well as on previously calculated outputs, which can be expressed by Equation 2.20 [20]. In this equation a_i coefficients are multiplied by the input values and b_i coefficients are multiplied by the previously calculated output values.

$$y[n] = \sum_{i=0}^{N} a_i x[n-i] + \sum_{i=1}^{N} b_i y[n-i] \tag{2.20}$$

These filters are useful because they can often be implemented with fewer coefficient, which avoids long convolutions, which makes it computationally efficient. However, due to the recursion the filter coefficient has to be carefully designed, since improper coefficient selection can lead to unstable system response.

2.9 I/Q Data

In many wave based signal processing systems, a convenient way to represent the received signal is by its in-phase and quadrature (I/Q) components. This approach is also fundamental to represent message signals in communication systems [21] and enables an efficient way to extract magnitude and phase information into a digital system with a relatively low data rate.

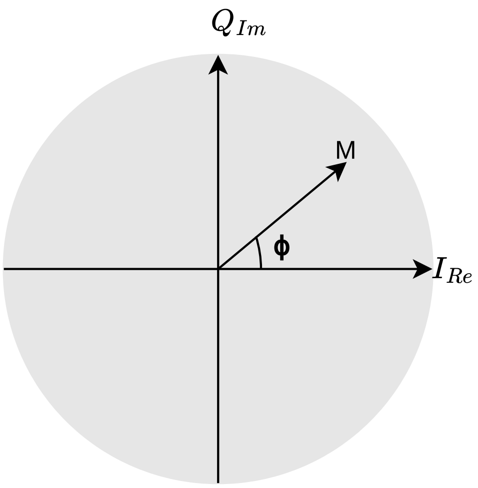

Figure 2.3: I/Q sample represented in the complex plane.

The received signal is mixed with two reference signals: one cosine (I) component and one sine (Q) component shifted by 90 degrees [22]. This process together with low-pass filtering, shifts the signal from the high operation frequency to two slowly varying base-band signals. Because of the orthogonality of the signals, these are together able to fully describe the magnitude and phase of the source signal. By then sampling the I and Q waveforms, the signal can be represented as points in the complex plane as in Figure 2.3. The magnitude is given by the distance from the origin and the phase is the angle between the sample and the positive I axis. The I/Q sample can also be used directly to calculate magnitude M and phase ϕ relative to the references using Equation 2.21 and Equation 2.22.

$$M = \sqrt{I^2 + Q^2} \tag{2.21}$$

$$\phi = \arctan(Q/I) \tag{2.22}$$

3
Method

The development process of the airspeed sensor will contain several steps. These steps will be divided into three main phases, progressing from a theoretical analysis to practical implementation and optimization.

The first phase will consist of a background study that includes a review of the most fundamental ultrasonic airspeed measurement methods, as well as a comparison of different transceiver alternatives. Furthermore, possible physical setups and control circuitry will be evaluated to identify requirements and constraints for the design. In addition, relevant algorithms for airspeed range extension and output filtering will be investigated.

The second phase will focus on prototype development. This phase will contain design and implementation of an electronic control circuit and a physical setup, with the goal to establish reliable interaction with the sensor modules. Another goal will be to enable evaluation of the sensor module's functionalities and to try out the most fundamental methods for airspeed calculation.

The third phase will be to implement and test selected algorithms and filtering techniques obtained from previous phases. These will be evaluated through practical experiment together with iterative optimization to ensure reliable and accurate airspeed estimation.

3.1 Control Circuit

The electronic hardware design will mainly consist of a microcontroller and a supporting circuitry which is required to be able to operate and interact with the transceiver modules. The design will be based on manufacturer recommendation, as well as previous experiences from earlier projects utilizing similar hardware.

An initial breadboard-based prototype will first be developed, serving as a testing and evaluation platform for different components. This will help verify reliable sensor interaction, with focus on minimal size, weight and power consumption.

The control circuit will then be implemented as a Printed Circuit Board (PCB), using KiCad [23], which is a open-source PCB design suite. This will reduce both weight and size of the circuit compared to a traditional breadboard implementation.

3.2 Mechanical Testing Rig

Much of the electronic hardware will be integrated into the drone body. However, a mechanical testing rig is needed to allow the sensors to be mounted in a more appropriate way for airspeed measurement and exposure to free airflow. This rig will be developed as a standalone prototype, since the integration to the drone is outside the scope of this project. However, the aim of the mechanical design will still be to demonstrate how compact the sensor mounts can be when integrated to the drone.

The test rig will be designed using Autodesk Fusion [24], converted to 3D printer code using PrusaSlicer [25], and then 3D printed by a Prusa MK4S [26]. This will ensure a more exact distance and angle between the transceivers. It will also make sure that the position of the sensor mounts are constant and that it will offer enough support during high airspeed testing.

3.3 Software

The microcontroller software is a key element in this project. It will control configuration and operation of the sensors. It will also produce real-time airspeed calculations by utilizing algorithms and digital filtering techniques. The software will be implemented on a RP2040 [27], which is a microcontroller marketed by Raspberry Pi, that will be able to run C programs using the C and Raspberry Pi Pico extensions in Visual Studio Code [28, 29].

3.3.1 Sensor Operation

From the software point of view, the sensors are controlled by a hardware specific C library or Application Programming Interface (API), called SonicLib [30] by TDK Invensense described in [31]. This library will control all sensor (CH101) specific tasks to produce and read measurements. The application specific tasks that will be performed by the library are:

- Initializing the sensor modules by loading appropriate firmware that will put the sensors in an application specific configuration.
- Control the measurement sequence by triggering the group of sensors
- Read from and write to the I2C bus, allowing retrieval of I/Q data for each sample at the receiver in a measurement.
- Change sensor settings during operation which makes it possible to switch between transmission and reception mode between measurements.

SonicLib is a platform-independent library, which means that the library is not developed for a specific microcontroller or development board. However, to be able to use the library with a microcontroller, a board support package is needed. This is a file or a package of files that acts as an interface between the library and the hardware on the board, and is needed to be developed for the RP2040.

3.4 Development of Airspeed Estimation Model

To be able to develop a robust airspeed estimation model, a thorough review of airspeed measurement methods, algorithms for range extension, and more general signal handling are needed. This will provide an understanding of the fundamental principles in airspeed measurement and how the airspeed measurement range can be extended, while maintaining reliable performance.

A review of hardware documentation is also needed to give an indication of what the sensor modules are capable of and what methods for airspeed extraction are possible to apply. However, experimental validation of the sensor modules will also be needed to fully asses the capabilities and limitations of the sensor modules for this specific application.

The following parameters will be investigated:

- Signal stability and continuity, evaluated by analyzing the phase difference of high magnitude samples between measurements under static airspeed conditions.
- Signal To Noise Ratio (SNR), analyzed by comparing phase stability and difference of magnitude in the received signal between zero airspeed and during applied airspeed.
- Synchronized phase, both between sensors and between sensor restarts, to understand if the sensors are using similar signals with similar phase for a specific sample or if it needs to be calibrated before a measurement can start.
- Waveform characteristics, to understand if the signal has a stable continuous frequency and magnitude, or varying behavior over time.

The insight gained from this evaluations will guide the development of the airspeed estimation model.

3.5 Data Processing and Visualization

The serial monitor built into Visual Studio Code is both able to show the data currently processed by the microcontroller through the RP2040 serial interface, and record it to a specific log file. The data will then be further processed and analyzed using Matlab [32], where visualization tools are used to both develop the functionality further and to show results of the airspeed measurements.

3.6 Digital Filter Development

The airspeed measurement relies on signals propagating through the air. This signal will both be affected by environmental disturbances and noise introduced by the hardware itself. To ensure reliable and stable airspeed estimation that can be processed by a control system, output filtering is needed.

Since the measured signal already is digitalized by the sensor modules, a digital filter will be developed and applied on the airspeed output value. The most important task for this filter is to attenuate high-frequency changes while preserving the information and trends in the airflow variations.

The filter will be designed and developed using MATLAB and its signal processing toolbox [33]. This enables a controlled development of the filter prior to implementation in the microcontroller software.

4

Design and Implementation

The complete sensor module consists of three main parts. First are the transceiver modules that generate measurement data. Second is the microcontroller software, which controls the transceivers and produces airspeed estimations. Lastly, a control circuit with level shifters, which enables communication between microcontroller and transceiver modules. The block diagram presented in Figure 4.1 shows an overview of the system. This chapter builds on this overview and provides a more detailed description of the complete sensor module, while also discussing the key design decisions and the reasoning behind them.

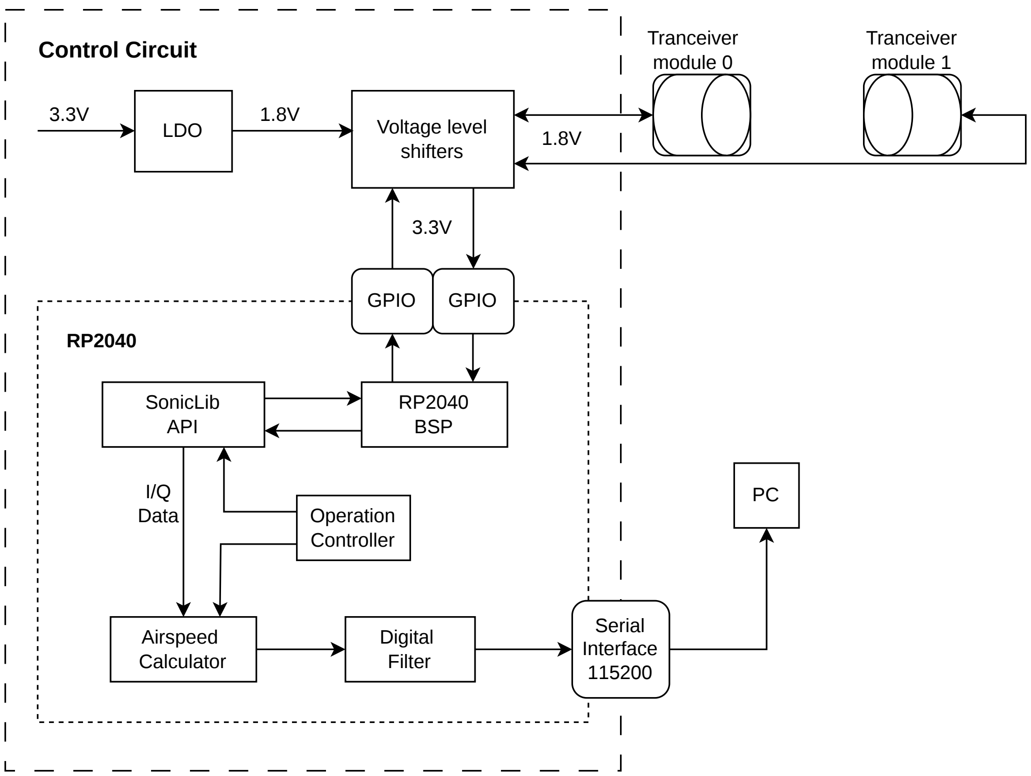

Figure 4.1: System overview.

4.1 Ultrasonic Transceivers (CH101)

The ultrasonic transceiver modules selected for this project are the CH101 [8] developed by TDK InvenSense. The CH101 module is a low cost and power efficient ToF ultrasonic range sensor based on MEMS technology. It has an distance measurement range from 4 cm to 120 cm, a typical operating frequency of 175 kHz, and operates at a voltage level of 1.8 V. The module has a piezoelectric micromachined ultrasonic transceiver and a SoC with internal signal processing and microcontroller, which provides ready-to-use data via the I2C bus. There are three types of data that can be extracted from the module [31]. Two of them are the calculated range, and the magnitude values based the SoC internal algorithms. The third type is the I/Q data that represents the sampled signal from each measurement, with each sample expressed as an in-phase and quadrature pair. Access to this level of detail was a key factor in the selection of transceiver module.

The CH101 module is available in different standard versions, one Pulse-Echo and one Pitch and Catch version. The specific module selected for this project is the EV_MOD_CH101-03-01 [34], which combines the two previously mentioned versions. This component consists of a transceiver module soldered on a circuit board with an omnidirectional acoustic housing and a flexible flat cable (FFC) connector. The board serves as an evaluation module for these kinds of transceivers, allowing for easier interaction and system evaluation.

4.2 Control Circuit Design and Components

The transceiver modules works with a voltage level of 1.8V, while the microcontroller works with 3.3 V. The control circuit is mainly built as an extension to the microcontroller board, allowing the microcontroller to interact with the transceiver modules, despite the difference in logic levels. Figure 4.2 presents a detailed view of the circuit and how the different components are connected.

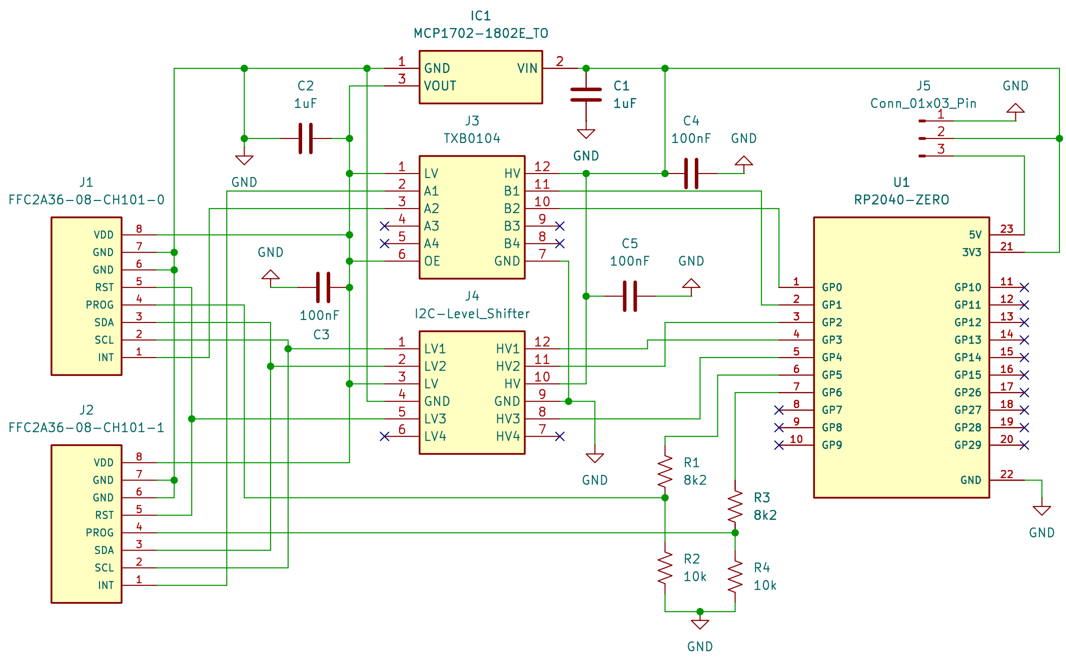

Figure 4.2: Schematic of the control circuit.

The control circuit consists of three main parts: The microcontroller board, which provides the I/O signals and is able to supply power to the control circuit, a voltage regulator that converts supply voltage to the required low voltage level, and lastly, different types of voltage level shifters tasked to translate logic levels between the ports of the transceiver modules and the microcontroller board. In addition, the control circuit also includes flat cable connectors to the transceiver modules and a connector for external power supply. This circuit design resulted in a PCB measuring 38 mm × 34 mm with a thickness of 8.8 mm, with components included.

4.2.1 RP2040 (RP2040 Zero)

The RP2040 [27] microcontroller is a central component of the complete airspeed sensor module, performing several key functions within the system. It was selected due to its potential ability to operate the ultrasonic transceiver modules through the SonicLib API and its clock speed of 133 MHz, enabling real-time airspeed calculations. In addition, it was also selected due to its ability to communicate with both transceiver modules and the autopilot system, running several communication interfaces at the same time.

There are several development boards based on the RP2040 with different functionalities and form factors. The Raspberry Pi Pico can be considered as the reference board for the RP2040, providing a well documented development environment. However, the RP2040 Zero board was selected due to its compact design while still preserving the performance and functionality of a Raspberry Pi Pico. In addition, this board offers 20 flexible I/O-ports, enough to interface with the transceiver modules and it provides the control circuitry with a 3.3 V voltage regulator.

4.2.2 Voltage Regulator

A low-dropout voltage regulator (LDO) is used to convert the 3.3 V, provided by the microcontroller board, to a stable voltage of 1.8 V, for the low-voltage transceiver modules. It is selected because of its simplicity, small form factor and low power dissipation for low power applications, compared to other voltage regulators. The efficiency (η) of an LDO can be calculated by Equation 4.1 [35]. Based on the equation, the efficiency depends on the dropout voltage, which is the difference between output voltage (V_O), input voltage (V_I) and the load current (I_L). It also depends on how large the quiescent current (I_q) is, compared to the load current.

$$\eta = \frac{I_L V_O}{(I_L + I_q) V_I} \times 100 \tag{4.1}$$

To minimize the power dissipation, it is important to select an LDO with low quiescent current, especially in low power applications where it will have a larger effect on the total dissipation. The selected MCP1702-1802E/TO [36] LDO has a quiescent current of 2 uA, which is negligible compared to the load current.

4.2.3 Voltage Level Converters

The level converters are used to achieve communication between the microcontroller and the transceiver modules that are working with different voltage levels. The choice of level converters for each I/O port depends on the functionality of the specific transceiver pin.

The two I2C pins, SDA and SCL are open drain, while the PROG and RESET pin are standard digital inputs without internal pull-up or pull-down resistors [37]. All these lines are compatible with conventional I2C converters with pull-up resistors. However, the PROG pin is active HIGH, meaning that a direct connection to a pull-up resistor would result in continuous power consumption when the pin is normally low. To avoid this, the PROG line is instead converted with a voltage divider, which reduces static power consumption, while still ensuring correct signaling. The other pins are connected via a level converter module based on BSS138 MOSFET transistors with pull-up resistors on both sides, allowing bidirectional communication while safely translating voltage levels.

The INT line is a unique circuit and needs special handling for level shifting. It is an active HIGH, bidirectional I/O, designed to operate with short HIGH trigger pulses in either directions, with an internal pull down resistor to restore the line to LOW after each trigger pulse [37]. Standard I2C level shifters would be unsuitable because of their pull-up resistors conflicting with the transceiver's internal pull-down resistors. This line is instead shifted with a TXB104, which is a push-pull level-shifter, capable of driving both HIGH and LOW in either directions. However, the pull-down resistor of the transceiver is too weak to reliably drive the line LOW against the TXB104 output. This is solved by the microcontroller software, which drives the INT line low after each HIGH pulse.

4.3 Transceiver Validation

As previously discussed in Section 3.4, an experimental validation of the transceivers is needed to understand the capabilities and limitations of the system, and to guide further development and design decisions. This section will present results from these tests, which were conducted with two transceivers pointed to each other at a distance of 32.8mm.

4.3.1 Phase Measurement Under Static Conditions

By analyzing how the phase evolves over time under static airspeed conditions, information about the signal stability and phase continuity can be obtained. To analyze this, phase measurements were conducted in still air. Figure 4.3 represents four measurement rounds, with system restarts between each round.

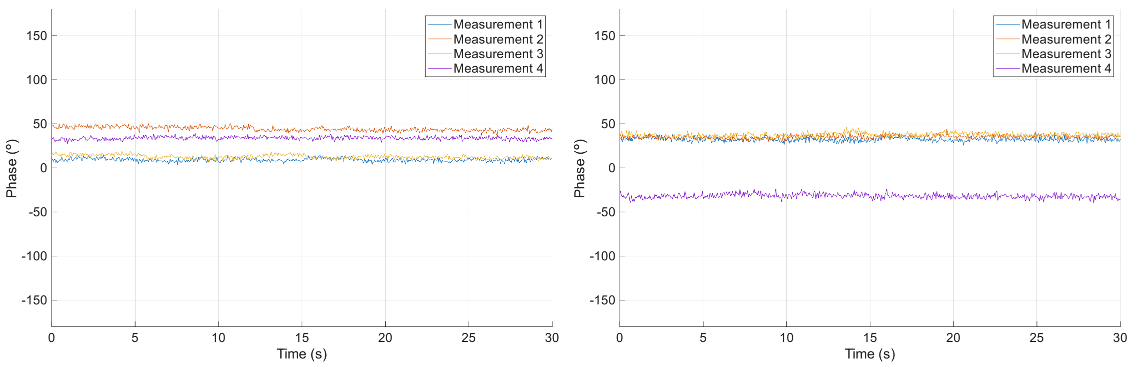

(a) Tranceiver 0 **(b)** Tranceiver 1

Figure 4.3: Phase under zero airspeed conditions

The graphs demonstrates a continuous phase signal with no observable drift and with minimal noise. However, the measurements also show that the phase differs between the two transceivers at the same sampling instance. Furthermore, as observed for each measurement in Transceiver 0 and measurement four in Transceiver 1, the phase may also vary between system restarts on the same transceiver. Although some degree of continuity can be observed between measurement rounds, the phase difference in between is too large to disregard the need of calibration under zero airspeed conditions at each measurement start-up.

4.3.2 Measurements Under Airspeed Conditions

The purpose of testing the transceiver under more than just zero airspeed is to both get an understanding of how the phase measurement performs during airflow, and how the signal magnitude is affected. Figure 4.4 demonstrates phase and magnitude response of the two transceivers under airflow conditions, with the transceivers placed in the direction of the airflow. This test utilized a hand held fan as the source of airflow when going from still air to a certain airspeed and back to still air again.

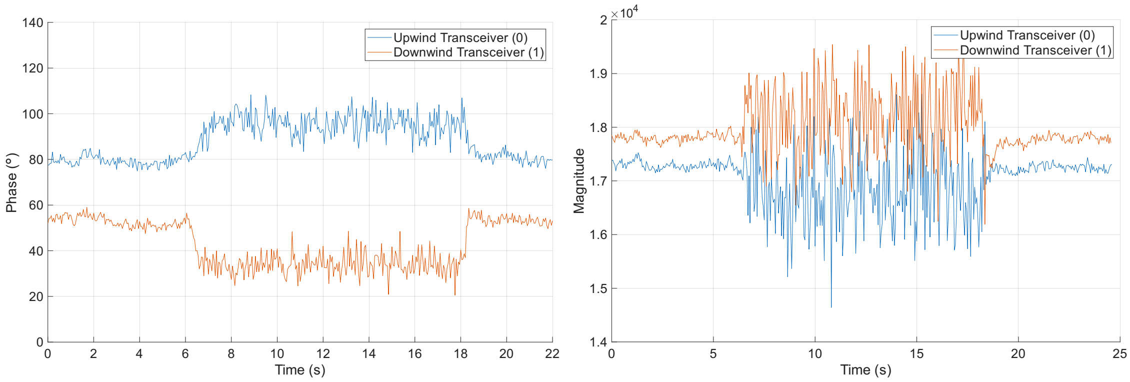

(a) Phase.

(b) Magnitude.

Figure 4.4: Measurements under non-zero airspeed conditions (0° relative to airflow).

Figure 4.4a illustrates the evolution of a phase in the upwind and downwind transceiver. From the graph, what can be observed is that both transceivers are affected by the airflow, with a clear phase shift and increased noise. Although the phase shift seems to be stable enough to be useful for airspeed extraction, what can also be observed is that the upwind transceiver exhibits less phase shift compared to the downwind transceiver. Figure 4.4b shows the magnitude during the same measurement. The magnitude levels are kept relatively high during the airflow segment, which indicates that the signal stays strong during airspeed conditions. However, the magnitude data is still noisy, where it is hard to find any stable trends for airspeed information in the low airspeed case.

Figure 4.5 demonstrates the phase and magnitude from a similar test, where the only difference is that the transceiver pair are placed in a 45° angle relative to the airflow. This setup forms a path of free airflow between the transceivers that is not as heavily affected by the appearance of the upwind transceiver.

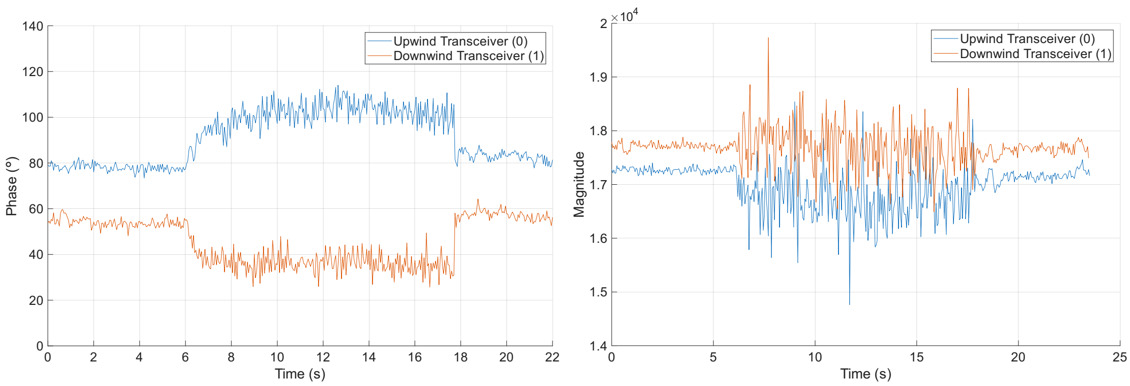

(a) Phase.

(b) Magnitude.

Figure 4.5: Measurement under non-zero airspeed conditions (45° relative to airflow).

This test demonstrates that even though an angled setup would introduce an angular component to the airspeed, the signals are still more phase shifted than the first setup, especially for the upwind transceiver. It also shows that the free airflow will have less noise introduced in both phase and magnitude relative to the total phase shift. However, the trends in the magnitude are still too vague to obtain stable airspeed information.

4.4 Mechanical Rig and Transceiver Positioning

The mechanical rig consists of a 1 mm flexible base plate with two extruding nobs working as transceiver mounts while diminishing the aerodynamic impact. These nobs have a diameter of 18 mm and extrudes 9 mm from the base plate. Figure 4.6 shows the transceiver positioning, relative to each other and to the direction of airflow.

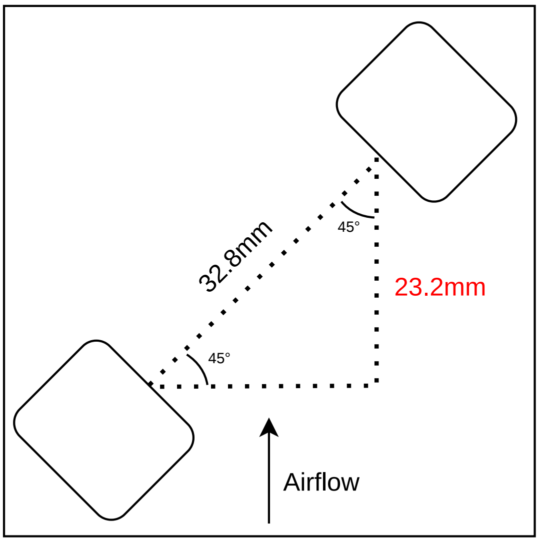

Figure 4.6: Transceiver positioning

The angular mounting of the transceivers is to leverage the benefits of free airflow, demonstrated in Subsection 4.3.2. Placing a transceiver in the signal path would create flow disturbances, thereby breaking the linearity of the airspeed equation. The two transceivers are facing each other with a distance of 32.8 mm, with an angle of 45° relative to the airflow. This creates a theoretical effective distance of 23.2 mm, where the airflow is able to impact the velocity of the sound waves. However, this does not take into account the impact that the transceiver mounts have on the effective airflow, which is something that requires testing to determine.

This configuration represents a design trade-off that allows for free airflow between the sensor modules while maintaining signal magnitude to facilitate reliable system testing. It also gives a theoretical airspeed range within one phase cycle, close to the maximum airspeed goal of the project.

4.5 Wind Tunnel Pre-test

Prior to the final testing, a pre-test of the ultrasonic airspeed sensor module was performed using a wind tunnel to evaluate the sensor against a controlled reference airspeed from 5 m/s to 25 m/s, in steps of 5 m/s. These tests made it possible to evaluate the evolution of the phase shift in the module, and a few other parameters against an actual reference speed. This section presents some of the data obtained from these pre-tests.

4.5.1 Phase Shift

To be able to translate the transceiver data into airspeed information, phase shift in relation to an actual reference speed is needed. Figure 4.7 shows the phase shift of the upwind and downwind transceiver during airflow, relative to a calibrated zero-phase.

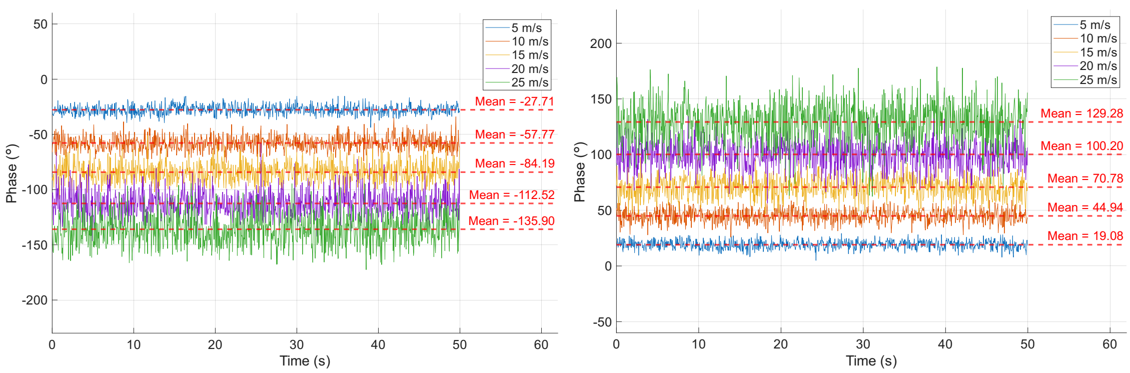

(a) Upwind transceiver (0). **(b)** Downwind Transceiver (1).

Figure 4.7: Phase relative to the reference airspeed.

The graphs demonstrate that the evolution of the phase shift value is lower compared to the expected theoretical value. This can be interpreted as that the effective distance is shorter in the area where the signal is affected by the airflow. This will also affect the airspeed range.

4.5.2 Magnitude Response

As described in Section 2.6.1, the magnitude of the received signal could possibly be utilized for range extension. Figure 4.8 and 4.9 demonstrate the evolution of a magnitude sample in the two transceivers during airflow.

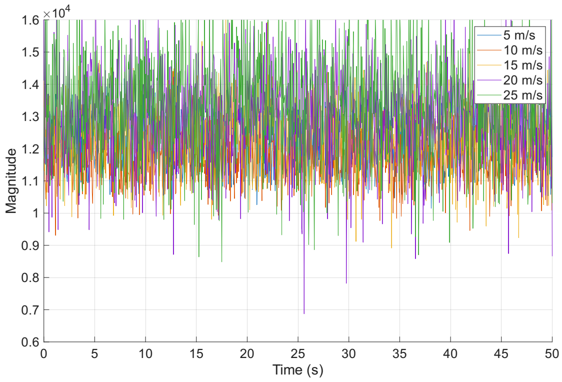

(a) Upwind transceiver (0).

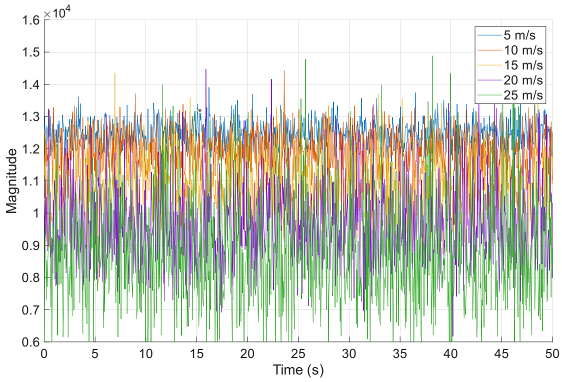

(b) Downwind Transceiver (1).

Figure 4.8: Magnitude relative to reference airspeed.

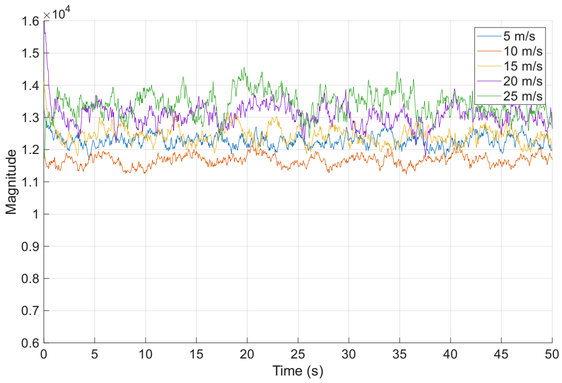

(a) Upwind transceiver (0).

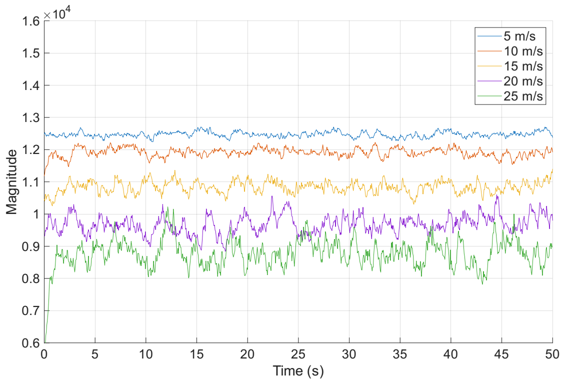

(b) Downwind Transceiver (1).

Figure 4.9: Filtered magnitude relative to reference airspeed.

The magnitude of the received signal in the upwind transceiver shown in Figure 4.9a does not show a clear relation between signal magnitude and increased airspeed. However, the magnitude of the downwind transceiver in Figure 4.9b shows the opposite behavior, with a clear trend toward decreasing magnitude with increasing airspeed. This indicates that there are no straightforward relations between magnitude and the airspeed in this sample for both transceivers. Nevertheless, with further investigation and testing, it is likely that additional information could be extracted.

4.6 Airspeed Estimation Model

The fundamental part of the airspeed estimation model is based on the phase difference method presented in Section 2.4. The two transceivers alternate between transmission and receiving mode. When one is transmitting, the other is receiving and vice versa. The phase is obtained from the I/Q data extracted during a receiver measurement cycle for each transceiver. It is represented as an angle between –180°

and +180°, where the sample with the largest magnitude from each transceiver is used.

Due to the inconsistent behavior of the phase between the transceivers and system restarts, as presented in Section 4.3.1, a phase calibration procedure is performed prior to the airspeed estimation start. This is done by performing several phase measurement cycles at zero airspeed, which produces a reference (zero-phase) for each transceiver. The airspeed value is then based on the phase difference between the calibrated phase and the phase measured during operation on both transceivers. The uncertainty of zero-phase also means that the phase wrapping could happen at an uncertain airspeed. When this occurs, the phase difference value will get an undesired value that is outside the one cycle limit. This is solved by a procedure that checks if the value is within the expected phase. If it is not, adjustments are applied to compensate for the phase wrapping.

Based on the phase difference method which is limited to one phase cycle, the measurable airspeed range is given by Equation 2.15. With the mechanical rig and the effective distance of airflow, this would result in a theoretical airspeed range of ±14.3 m/s. Most similar systems in literature are either built for anemometry or flow measurements, both of which assume flow in both directions. This is what the theoretical calculations also are built upon. However, in reality this range is possible to shift as long as it is within one phase cycle. In the system developed in this project, the airspeed range is shifted by adjusting the boundaries to what is seen as the expected phase in the phase wrapping procedure. For a fixed-wing drone application, it could be assumed that the airflow is mainly in one direction, since the drone must maintain positive velocity in order to generate lift. If the airflow is assumed to be only in one direction, the airspeed range could be moved to a maximum positive range of 0–28.6 m/s.

Other methods for range extension have been explored by, for example, utilizing the information in the magnitude response as presented in Section 4.5.2, and by utilizing frequency information of the received signal. These parameters would likely not be able to produce exact airspeed information, but possibly be able to guide the phase difference method over the one cycle limit. Another method explored is the phase-tracking algorithm presented in Section 2.6.2. Although the method seems to perform well under stable conditions, aggressive filtering will be required in a drone application, as rapid phase variation and disturbances introduce risks of incorrect phase wrapping.

However, discoveries from the experimental results in the first wind tunnel test presented in Section 4.5.1, show that the phase is less affected by the airflow than expected. If this is only to be interpreted as the effective airflow distance, it would be about 9.5 mm, based on the mean values of phase shift at a certain airspeed. This instead leads to an actual airspeed range within one phase cycle of ±34.7 m/s or a maximum positive range of 0-69.4 m/s. Due to these findings, the maximum airspeed goal of 25 m/s is theoretically already fulfilled within one phase cycle. Applying other methods for range extension would add uncertainty to the airspeed value, since the one phase cycle method seems to be the most robust method that could recover from measurement errors and handle larger phase jumps. By shifting the measurement window to a range of -14.4 to 55.0 m/s, the system can capture and measure higher peak airspeeds and also handle airspeeds close to 0 m/s and bidirectional wind gusts, even with the presence of disturbances.

4.7 Output Data Handling

The raw estimated airspeed output (V) is processed by a signal handling stage with the primary purpose to suppress outliers and high frequency noise, while still preserving overall trends and system responsiveness. First, the airspeed value is passed through a median filter that removes large outliers caused by single erroneousness measurements, or large noise that do not belong to the underlying trend of the data. The value is then processed by a low pass filter to attenuate remaining high frequency changes and create a stable output that can be used for further processing and control applications.

The median filter is built on a comparison based sorting algorithm, putting the windows of samples in order such that the median value can be selected. Equation 4.2 shows how the algorithm is applied on a 3-sample window, containing the current and the two previous samples obtained from the airspeed estimation model, which generates a median airspeed (V_{med}).

$$V_{med}[n] = \text{median}(V[n], V[n-1], V[n-2]) \tag{4.2}$$

A median filter introduces a delay in the system, which increases with the size of the sample window. This algorithm is only using a 3-sample window, since it is sufficient enough to remove single outliers while limiting the filter delay to maximum two samples.

The median filtered airspeed estimate is then further processed by a single pole IIR low-pass filter, which uses the first two coefficients in the IIR filter equation expressed in Section 2.8. Equation 4.3 shows how the filtered airspeed (V_{filt}) is generated, where the current median airspeed estimate ($V_{med}[n]$) acts as the input to the filter, while the previous output value ($V_{filt}[n-1]$) is used as feedback in the recursion.

$$V_{filt}[n] = a_0 \times V_{med}[n] + b_1 \times V_{filt}[n-1] \tag{4.3}$$

The filter coefficients are defined by the tuning parameter α, which has a value between 0 and 1, where a_0 is equal to α, and b_1 is equal to $1 - \alpha$. The parameter α therefore controls the weighting between the current input sample and the previous filter output. α is set to 0.2 to provide high noise attenuation, while preserving the output responsiveness.

4.8 Output Rate

The output rate of the ultrasonic airspeed sensor is limited by the speed of the ultrasonic transceiver modules, and is reported to be maximum 100 Hz. This means that the maximum output rate of the sensor module is just below 50 Hz, including two phase measurement loops and extra computational time. Extensive testing has showed that these values almost match the theoretical, where a phase measurement takes about 10 ms with only minor differences between measurements. However, the software has been limited to an maximum output rate of 20 Hz, accounting for the uncertainty of the individual phase measurements, while still meeting the target output rate of this project. To prevent system failures, the software does not prohibit longer measurement cycles from occurring.

5
Results

This chapter presents the results from a series of tests evaluating the ability and performance of the sensor module to accurately measure airspeed. It also provide supplementary measurement and estimation data, such as weight, power consumption and cost estimation, needed for the overall evaluation of the module.

5.1 Cost Estimation

Table 5.1 presents the quantity and the estimated cost of each component required to build one complete sensor module. Since the components used in the project were acquired through different suppliers and vendors, including existing inventory and academic resources, the prices of the components presented in the table are not fully reflecting the exact purchase costs of the developed prototype. Instead, the table provides standard unit prices for the components from accessible vendors, intended to represent a cost example. Factors such as shipping costs, duties and taxes are excluded from the list, since these may vary depending on order volume and other purchase conditions. The cost of the mechanical rig is also excluded, since the 3D printing has been performed with academic resources. Furthermore, that material cost is marginal and does not significantly affect the overall cost.

Quantity	Item	Cost (SEK)	Vendor
2	EV_MOD_CH101	175	Mouser
2	FFC/FPC 8Pos (cable)	33	Mouser
2	FFC/FPC 8Pos (connector)	5	Mouser
1	TXB104 (4-channel)	32	Mouser
1	MCP 1702 LDO	6	Mouser
1	RP2040-Zero	48	Amazon
1	I2C level shifter (4-channel)	9	Amazon
2	10 kOhm Resistor SMD	2	Mouser
2	8.2 kOhm Resistor SMD	2	Mouser
2	1 uF Resistor SMD	2	Mouser
2	0.1 uF Resistor SMD	2	Mouser
1	PCB	19	JLCPCB
	Total Cost:	556	

Table 5.1: Cost estimation for one complete sensor module.

Table 5.1 shows that the transceiver module with its associated flat-cable accounts for the majority of the total cost, while the PCB specific component constitute less than one third of the total cost.

Among the PCB specific costs, the RP2040-Zero board, the TXB104 board and the PCB itself contributes the most, while the other level shifter, regulator and passive components contribute marginally.

5.2 Zero Airspeed Test

Due to the varying starting phase of the sensor module, a zero airspeed test was performed to evaluate how well the phase was calibrated. By also measuring the airspeed after a high load with large airspeeds and rapid changes in the airflow, the effect on the hardware could also be evaluated. Figure 5.1 presents an error bar graph for these tests, where the airspeed measurements were recorded over a period of at least 250 seconds. In the graph, the blue bar represents the minimum and maximum span of the measurement, the orange bar represents the standard deviation, and the dot represents the mean value for each measurement. The first three readings correspond to measurements performed immediately after the start-up phase. The last three measurements were taken immediately after exposure to high airflow, during which the sensor module was exposed to airflow for 20 seconds using a hairdryer with an estimated airspeed of between 15 m/s and 20 m/s.

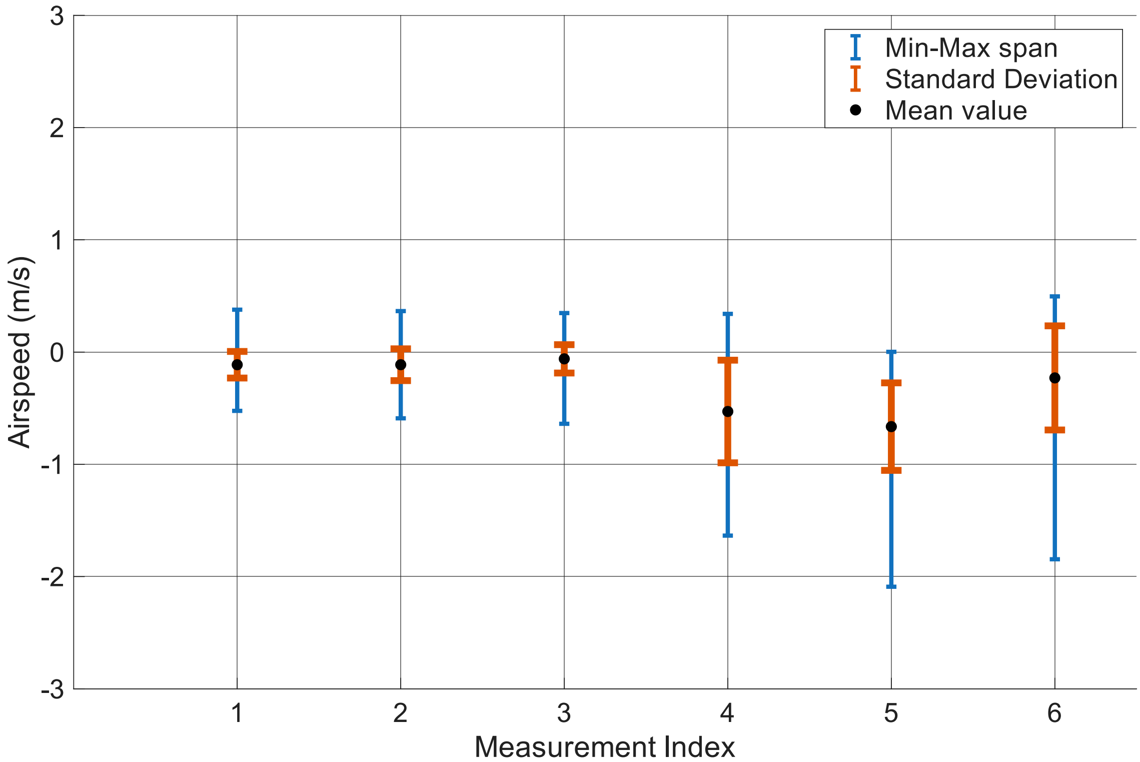

Figure 5.1: Error bar graph based on data from zero airspeed test.

The error bar graph in Figure 5.1 indicates that the calibration procedure is highly accurate, where the maximum deviation of the mean value is 0.11 m/s in the start-up measurements. What can also be observed is that the system has an inherent measurement fluctuation of about ±0.5 m/s, even in still air. Moreover, the standard deviation indicates that the main part of the measurements exhibits an even smaller spread. In the later measurements, the graph also shows that high airspeeds actually affect the hardware, where the mean and minimum airspeeds have drifted lower than the earlier measurements. Figure 5.2 shows how the airspeed evolves over time for one of these data sets.

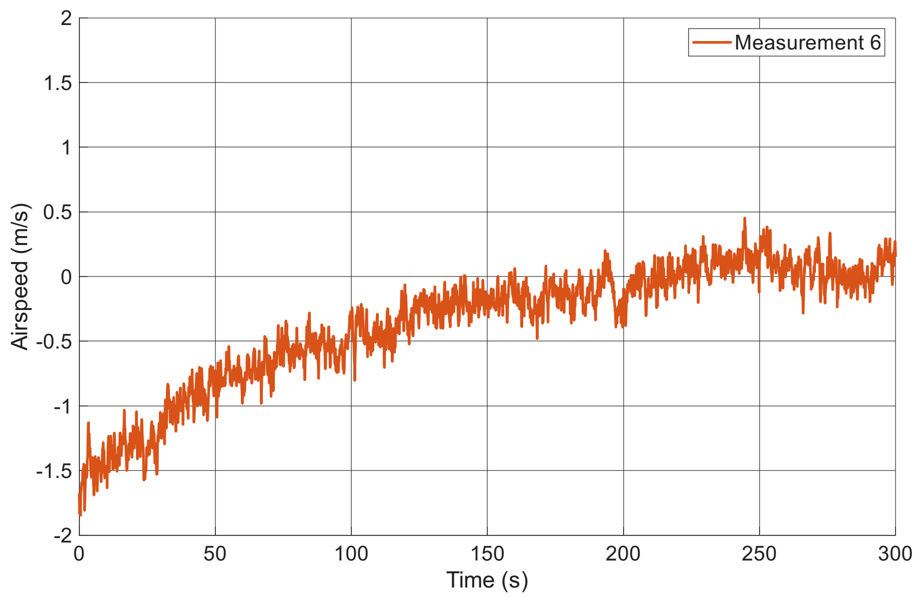

Figure 5.2: Recovery from rapid decrease in zero airspeed test.

Figure 5.2 demonstrates the reason why the error bars at the higher indices in Figure 5.1 are drifted lower than the earlier ones. What can be observed is that the airspeed measurement is pushed lower than zero after a rapid decrease of airspeed, but is recovering over time. Figure 5.3 shows the phase response of the same measurement.

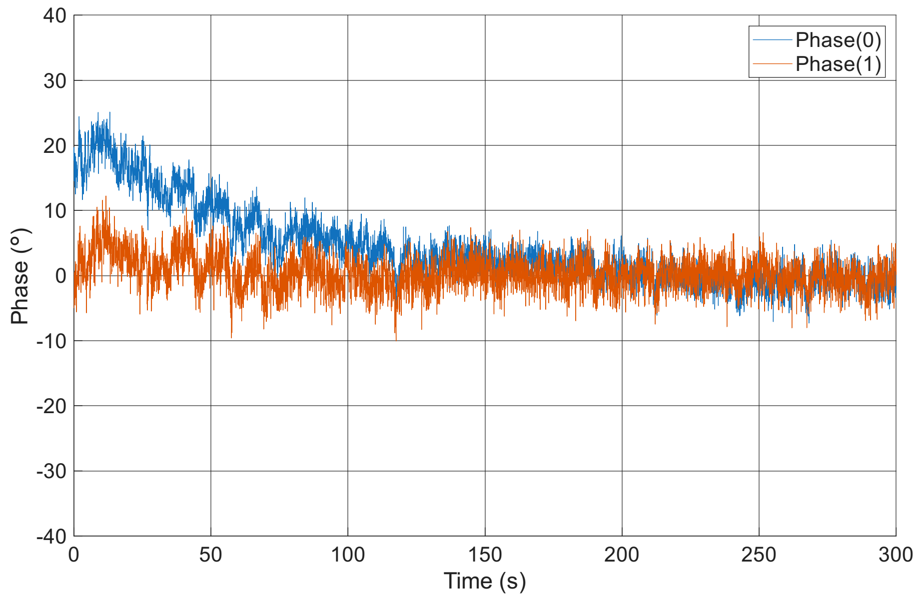

Figure 5.3: Phase response of the recovery in zero airspeed test.

An observation of the phase reveals that transceivers are not equally affected, where the phase measurement from the upwind transceiver is showing a larger drift than what is shown from the downwind transceiver.

5.3 Wind Tunnel Airspeed vs Sensor Measurement

To evaluate the accuracy of the ultrasonic airspeed sensor module, a final test was performed using a wind tunnel provided by Chalmers Laboratory of Fluids and Thermal Science. The wind tunnel provides a controlled environment, where a set airspeed can be assumed as the actual airspeed. The test was performed by letting the sensor module measure five different controlled wind velocities, ranging from 5 m/s to 25 m/s in steps of 5 m/s. Figure 5.4 presents an error bar graph for these tests, where the blue bar represents the minimum and maximum span, the orange bar represent the standard deviation and the dot represents the mean value for each measurement. Each velocity was measured two times with system restarts in between. The time of the recordings for each velocity exceeded at least 150 seconds and the output rate of the sensor module was 20 Hz during the complete test.

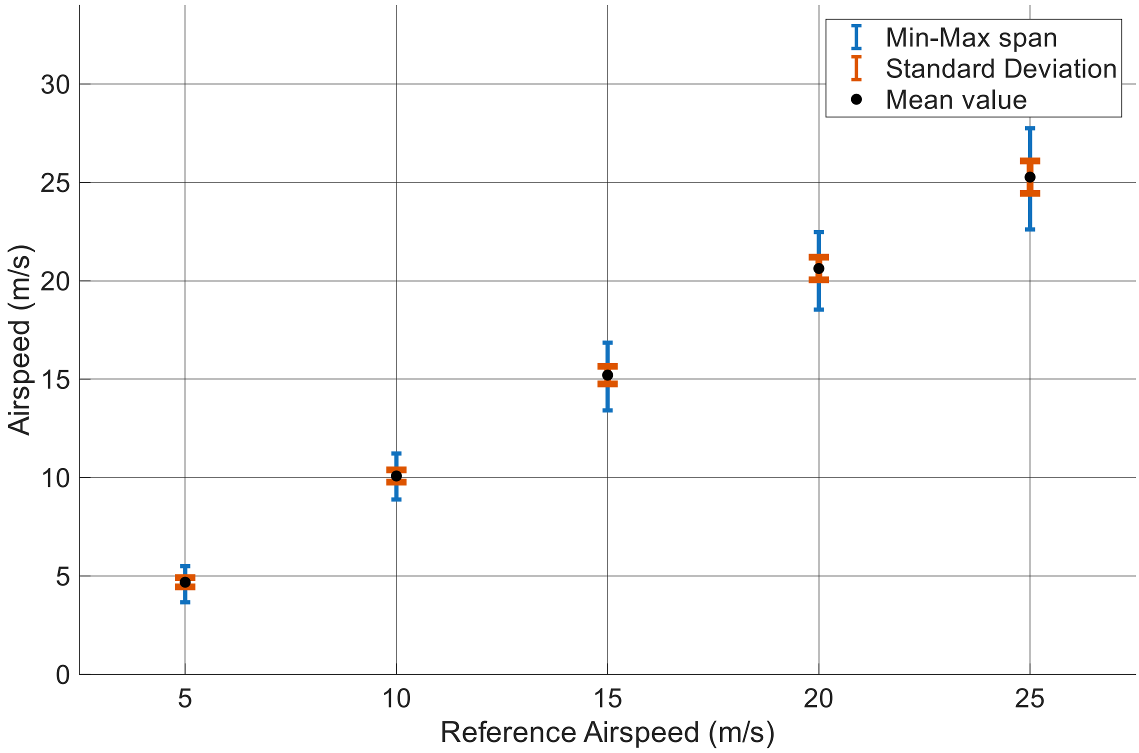

Figure 5.4: Error bar graph based on data from wind tunnel test.

The error bar graph demonstrated in Figure 5.4 shows that the airspeed could be measured with high accuracy over the complete range. Table 5.2 presents a summary of the airspeed data produced during the test, where the largest mean error occurs at the 20 m/s measurement, with an offset of 0.63 m/s from the true value. The measurement errors were also within the ±3 m/s limit, where the maximum error was +2.76 m/s at the 25 m/s measurement. Furthermore the standard deviation shows that the majority of the measurements are more tightly distributed around the mean value, with a maximum value of 0.82 m/s, suggesting that the typical errors are even smaller than the worst-case.

Actual airspeed (m/s)	5	10	15	20	25
Minimum	3.66	8.82	13.42	18.54	22.61
Mean	4.68	10.08	15.21	20.63	25.27
Maximum	5.50	11.24	16.86	22.48	27.76
Standard deviation	0.24	0.31	0.45	0.57	0.82

Table 5.2: Summarized data from wind tunnel test.

5.4 System Dynamics

Testing the response time and the system's ability to handle rapid changes allows for the system to be validated under more dynamic circumstances. Figure 5.5 presents a graph of how the system responds to rapid airflow, where the blue line represents the calculated airspeed based on raw phase, and the orange line represents the output, filtered airspeed. A hairdryer is used as the source of airflow. This is used with the same speed setting in two directions.

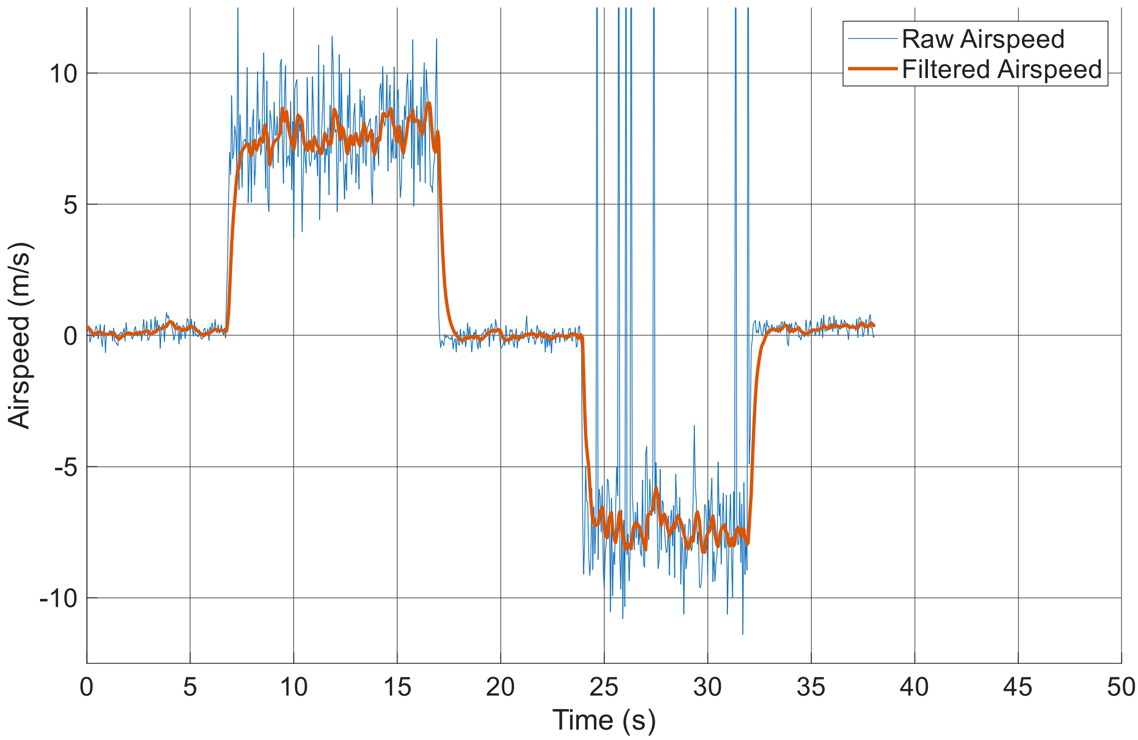

Figure 5.5: Measurement response on rapid changes in airspeed.

The graph in Figure 5.5 shows that the system is able to handle rapid changes in two directions without miss-calculations. It also shows that the raw airspeed starts to flip when it reaches the limit of the negative velocity, which is expected. It then stabilizes at a value close to zero again.

A common metric used to evaluate responsiveness of a system is to obtain the response time in its step response. The rise time is typically defined as the time required for the measurement to transition from 10 % to 90 % of the steady state change. Respectively, the fall time is the time required for the measurement to transition from 90 % to 10 %.

Since it is not possible to create an instant airspeed change, an ideal accurate step response is not possible to produce in the reality. However, the response from the rapid airflow change can still be sufficient enough to evaluate the system, even though it will not give perfect data. Figure 5.6 demonstrates a step response test, where the average start and end speed is obtained from red dotted lines and the 10% and 90% co-ordinate is marked in the slope of the rising airspeed.

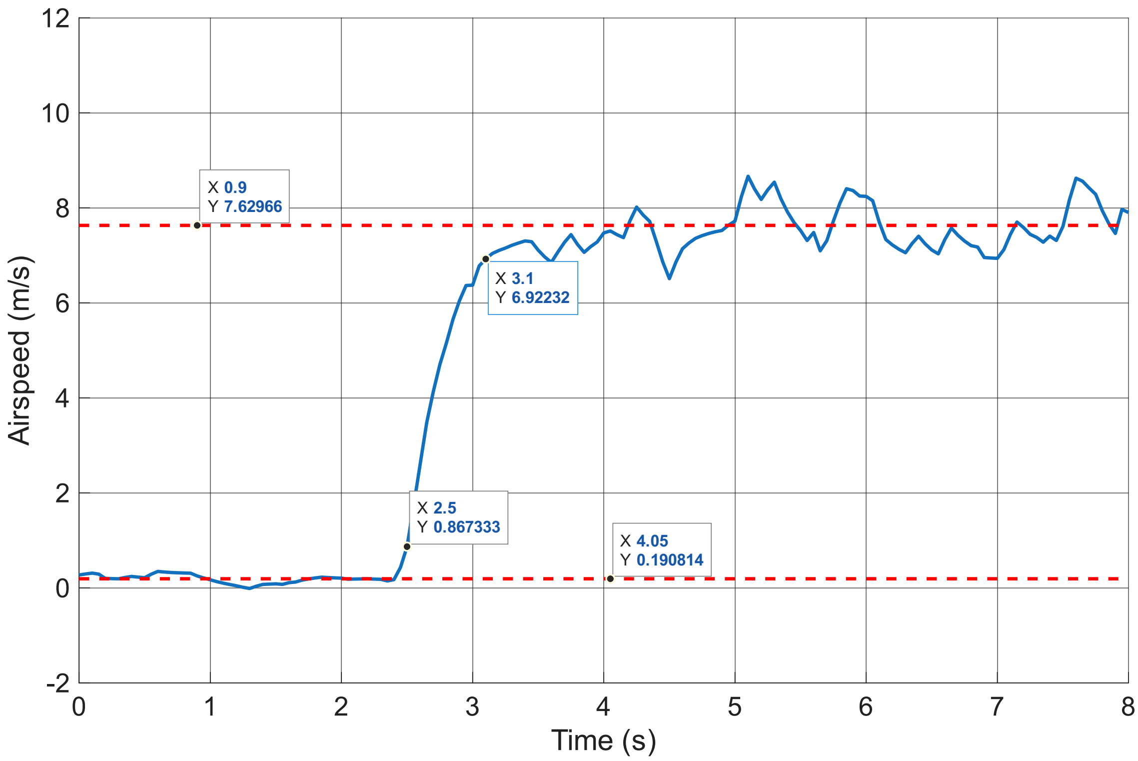

Figure 5.6: Step response field test, to calculate response time.

From Figure 5.6, a rise-time of 0.6 seconds can be obtained. Table 5.3 below presents rise and fall times obtained from three different step tests with three different airspeeds.

Airspeed step size	Rise time (sec)	Fall time (sec)
0.19-7.63 m/s	0.60	0.50
-0.01-10.50 m/s	0.50	0.45
0.18-15.76 m/s	0.50	0.50

Table 5.3: Response time from three different step tests.

What can be observed from Table 5.3 is that the rise and fall time produces similar results even with different sizes of steps. This result indicates that the system behaves in a linear manner, where the system responds consistently to different loads.

5.5 Power Consumption

To analyze the power consumption during operation of the sensor module, a multimeter is used to measure average current, and voltage is assumed to remain constant at its nominal value. The measurements are separated in to two parts: Measuring at every active output of the RP2040 microcontroller board (3.3 V), called application-specific electronics, and measuring from an external power supply to the RP2040-Zero power input (5 V), called the total system. This makes it possible to separate the power consumption of the application specific electronics from the power consumption of the microcontroller board.

Since the RESET and PROG pins are used only during the sensor initialization and not during operation, the current will not be measured from them. Furthermore, since all the GPIO ports that are left operate bidirectionally, accurately measuring the current flowing from the microcontroller becomes complex. Therefore, the entire measured current on the GPIO pins is treated as consumption, which will provide a worst-case estimation.

Table 5.4 shows the measured current of each active GPIO and 3.3 V power supply from the RP2040 zero. It also shows the current measurement of the total system, where the current consumption is measured between an external power supply and the RP2040 board 5 V power input. The table shows three different values for each measurement based on the multimeter's three different ways of measuring current (DC, AC and AC+DC).

Source	DC	AC	AC+DC
3v3 Power Supply	0.39 mA	0.57 mA	0.68 mA
GPIO 0 INT 0	0.25 uA	0.76 uA	0.80 uA
GPIO 1 INT 1	0.26 uA	0.82 uA	0.81 uA
GPIO 2 SDA	0.054 mA	0.137 mA	0.149 mA
GPIO 3 SCL	0.064 mA	0.131 mA	0.144 mA
Total	0.508 mA	0.840 mA	0.975 mA
Total System (5V)	30.55 mA	0.80 mA	30.57 mA

Table 5.4: Measured current during operation

Following the worst-case estimation approach, considering the combined AC + DC current measurements, the application specific electronics have a total power consumption of 3.3 mW. It is evident that the 3.3 V supply pin accounts for the most power, measured at 2.45 mW. In comparison, the I2C pins (SDA and SCL) are measured to be less than half of this value. The two INT pins contributes negligibly to the total power consumption of the external components, as their measured values are much smaller compared to the rest.

Considering the current measurement of the total system, it has a power consumption of 100.9 mW. This means that the microcontroller board accounts for a power consumption of approximately 97.6 mW, and that the sensor specific electronics will constitute a fraction of the total power consumption in this setup.

5.6 Weight

A weight analysis will not provide an exact representation of the final product weight mounted on a drone, which will be the most relevant metric. However, it provides an indication of the weight contribution of the different parts needed in the sensor module.

Part	Weight (g)
PCB	11.0
Mechanical Rig	4.1
2x Transceiver + Flat-cable	0.7
Total	15.8

Table 5.5: Weight of the different parts in the sensor module

Table 5.5 demonstrates the summarized weights of the different parts in the sensor module. What can be observed is that the PCB constitutes the largest part of the total weight, while the mechanical rig and transceiver plus flat-cables represents a small fraction of the total weight.

6 Discussion

The main goal of this project was to develop a sensor prototype that was able to measure airspeeds up to 25 m/s, with an accuracy of ±3 m/s, and do this with an output rate of 20 Hz. The aim was also to reach similar numbers in power demand, weight and cost, compared to the sensor that is currently used on the drone. This section contains discussions about the strengths and weaknesses with the developed sensor module and whether the goals have been fulfilled or not. It also contains discussions regarding different ways to interpret the results and suggestions on how to improve.

6.1 Measuring Airspeed

Only using the theoretical calculations, the airspeed range for the sensor module could have been met with the phase difference method, but only with a small margin. To truly reach stable measurements while dealing with a noisy environment from 0 m/s to 25 m/s, other methods and algorithms most likely would have been needed.

However, valuable insights regarding the effective airflow distance and the maintenance of stability with a very small effective airflow distance were obtained from the first wind-tunnel tests presented in Section 4.5.1. These insights prove that the airspeed range can be larger than expected, even within the one phase cycle limit. It made it possible for the theoretical calculation to extend the range from −14.4 m/s to 55.0 m/s, which fulfills the range goal of this project by large margins.

The resolution of the airspeed measurement depends on many different parameters, such as internal delays of the hardware and the degree of synchronization that can be established between the transceivers. Therefore, a theoretical value is difficult to calculate. Nonetheless, the results presented in Section 5.2 show that the system has a resolution of about ±0.5 m/s when the signal is flowing through still air. The results presented in Section 5.3 show that this value increases with applied airspeed, while still staying within a maximum value of ±3 m/s, up to a true airspeed of 25 m/s. With the achieved accuracy of the measurements, the system meets the goal of measuring airspeeds up to 25 m/s in one direction with a maximum error margin within ±3 m/s, at least in a controlled environment. It is worth noting that this analysis reflects a worst-case perspective. If the worst outliers would be disregarded, the standard deviation indicates that the typical measurement performance is likely to be even better.

6.1.1 Variations in Speed of Sound

The system is not built to take into consideration the environmental impact on the speed of sound. Since a lower temperature decreases the speed of sound in air, it will also decrease the airspeed range in the phase-based calculations. To illustrate this, an airspeed measurement in -20 °C, approximately the minimum expected operating temperature for the sensor, would decrease the maximum positive airspeed range from 69.4 m/s, in room temperature, to 60.2 m/s. This could be compensated for in a fairly simple manner by changing the speed of sound in Equation 2.15 according to the output of a temperature sensor, since large temperature changes result in relatively small changes within the measured airspeed range.

Nonetheless, the main problem appears because of the impact that the change in speed of sound has on what is defined as the zero phase, where the speed of sound in still air in the same example will shift from 343 m/s to 319 m/s. The shift in airspeed causes a fairly large shift in the phase, of about 124.5 °, without including the range shift that also will have an effect on it. This shows that the temperature will have a large impact on the airspeed estimation model and that it sets higher demands on temperature measurements. Although, the temperature should not limit the airspeed range enough to not reach the goals.

There are other environmental factors that can impact the speed of sound. Humidity is an example, although, it can often be neglected since the effect is very minimal in comparison. As described in Section 2.3, the dominant factor affecting the speed of sound is the temperature. To compensate for other factors, more specific testing and complex compensation will be needed.

6.1.2 Phase Drift by Rapid Changes.

The results presented in Section 5.2 show that the hardware actually is affected by the airflow itself, where high winds and rapid changes contribute to a drift in the calculated airspeed. This drift will most likely have a fatal impact on the basic functionality of the sensor if it is exposed to high airspeed in a harsh environment during a long period of time.

To really find the cause of this behavior, further investigation and testing is needed. However, as also observed in the results, the phase of the two transceivers are affected very differently. This may indicate that only one sensor is really causing the phase drift in both its reception and transmission, where the downwind and upwind transceiver otherwise would have been similarly affected. One possible explanation to this is that the downwind transceiver is hit by the direct wind flow into the vibrating membrane of the module, which means that this impact is causing the drift, while the upwind transceiver is protected by the transceiver mount itself.

A potential solution for this could be to build a transceiver mount that protects the acoustic port to the vibrating membrane, while not disturbing the free airflow between the transceivers.

6.1.3 Output Rate and System Responsiveness

The sensor module has maintained an output rate of 20 Hz during the complete testing procedure, showed in Sections 5.2, 5.3 and 5.4, showing that the output rate design goal has been achieved.

The system dynamics must be analyzed further to really evaluate the system responsiveness. The results presented in Section 5.4 show a response time of about 0.5 seconds, which implies that it requires about half a second to fully adapt to a change in airspeed. Something that is not included in these calculations is that the median filter also can delay the response time further by maximum two samples, equivalent to 0.1 seconds. This response time limits the sensor to capture airspeed fluctuations to some extent, which is something that can be interpreted as both positive and negative in a trade between stability and responsiveness.

Although, the signal handling part of this system is just one example of how the filtering procedure can be applied to reach acceptable results while maintaining some responsiveness. It could likely be modified to better integrate with the autopilot system. For example by filtering less aggressively, since autopilot systems often utilizes their own sensor fusion filters.

6.2 Design-Specific Evaluation and Comparison

Comparisons of the more design specific parameters can be complex to execute, particularly between the ultrasonic sensor and the currently used sensor (DLVR-L10D). This is because the ultrasonic airspeed sensor is developed as a standalone unit, where the complete control and processing chain is performed locally. The bare DLVR-module on the other hand just measures pressure differences, with the measured data often being processed by an external control unit as an autopilot.

Therefore, the comparison can be based on several different system-level approaches. The ultrasonic sensor can be considered as a fully standalone unit, as implemented in this project, including the internal control unit. It could also be assumed that all control tasks are transferred to a central control unit, leaving the sensor module only to contain sensor specific hardware. Similarly, the DLVR-module could be viewed either as a bare pressure transducer, just providing pressure data, or as part of a complete system producing ready to use airspeed data. Determining the most fair and appropriate comparison approach is not straightforward, since the ultrasonic sensor without internal control places higher demands on the central control unit compared to the plain DLVR-module. At the same time, it should be noted that it is a prototype that is compared to a fully developed product.

6.2.1 Weight and Size

A fair way to compare the ultrasonic airspeed sensor with a DLVR-module in terms of weight and size is by comparing it with the 3DR CAN airspeed sensor DLVR - M1009 [38], which is a DLVR-based airspeed sensor. It is developed as a standalone unit, with internal control, but still with a compact design.

The total weight of the DLVR-module is 12.2 g which is slightly lower than the total weight of the ultrasonic module (15.8 g). The largest weight difference origins from the difference in the PCB part, where the DLVR-module has a weight of just 3 g, while the ultrasonic module has a weight of 11 g. By comparing the other more mechanical parts, the ultrasonic module already seems to be just as weight-efficient as the DLVR-module.

The physical size of the complete sensor modules is more complex to compare, as the modules are based on different technologies. When considering only mechanical or physical footprint, beyond PCB related components, The DLVR-based solution is hard to beat, as it typically requires only a small tube inlet to be exposed to airflow. In contrast, the ultrasonic module requires exposed components protruding from the drone body. However, this project proves that this can be done in a more discreet way. When considering the size of the PCB, the DLVR-module also has smaller lateral dimensions compared to the ultrasonic module. Although, it is slightly thicker. The DLVR-based PCB measures 18 mm $\times$ 19.3 mm $\times$ 13.5 mm, while the ultrasonic based PCB measures 38 mm $\times$ 34 mm $\times$ 8.8 mm. The main difference could probably lie in the level of integration, where the DLVR-module utilizes more integrated components, enabling a more compact design.

To decrease the weight and size of the PCB further while maintain all the functionality, a more integrated design is needed, especially by integrating the microcontroller to the actual circuit board instead of using an extension board. This same procedure could also be done for the voltage level shifters. This would potentially both decrease the size of the actual circuit board and the weight of the components mounted, which at least would have decreased the total weight with a few grams, matching the weight of the DLVR-module and potentially decrease the size to the same level.

6.2.2 Power Consumption

The ultrasonic airspeed sensor requires 3.3 mW when the power consumption of the microcontroller board is not included. In contrast, when also considering the microcontroller board, the total power consumption increases to 100.9 mW. Since the microcontroller board consumes such a large portion of the total power consumption, it indicates that the micrcontroller board is not the most optimal solution from an power-efficiency perspective. The power consumption could probably decrease by integrating the microcontroller directly to the PCB which would avoid unnecessary peripherals. It could also most likely be done by optimization of the code with different power saving functions. However, it would not be enough to match the rest of the electronics, since the RP2040 is not built for extreme low power applications. To really make a difference, implementation of a low power micro controller is needed. The control functionality could also be moved to the central control unit instead.

The total power consumption can still be compared with the same type of standalone DLVR airspeed sensor as discussed in Subsection 6.2.1. These devices are reported to operate with a voltage of 5 V, with a current consumption of 60-100 mA, which results in a power consumption between 300-500 mW. This is actually higher than the ultrasonic system, with the RP2040-Zero included.

The bare DLVR-L10D sensor module itself is able to operate at a Voltage of 3.3 V and a current of 3.5 mA [9], resulting in a power consumption of 11.55 mW. This value has been compared to the power consumption of one of the earlier developed prototypes, where the power consumption was reported at a lower value of 9.5mW [4], without control unit included. Both these values are still higher compared to the ultrasonic airspeed sensor without the microcontroller included, showing that this solution with an ultrasonic MEMS can be very power-efficient in comparison, as long as a more power effective solution for the sensor control can be made.

6.2.3 Cost

The prices of DLVR-modules ranges from 450 SEK, for the cheap bare models, to above 2000 SEK, for standalone models with internal control and communication. The total cost of the ultrasonic sensor module presented in Section 5.1 does not necessarily reflect the exact cost of a finalized product. Several additional costs would have needed to be accounted for in its production, while the costs of a number of components could likely been reduced through further design optimization. For example, the cost of the most expensive component could potentially be reduced by more than half by using the standalone transceiver modules instead of the evaluation boards. This highlights some of the uncertainties associated with a final cost estimation but it also indicates that the ultrasonic module at least could fall into the same price range as the DLVR-modules.

6.3 Aerodynamic Issues

There are several potential difficulties with these kinds of sensor modules related to the aerodynamics and how the air is able to propagate between the two transceiver modules. The current setup has focused on controlled forward-facing airflow without concerns for the angular airflow from sharp turns and wind gusts.

Theoretically, with the current angular mechanical setup that introduces an angular component in the airspeed calculations, two sensor modules are needed to compensate for angular airflow. In practice, the situation is much more complex, as transceiver modules themselves have substantial impact on the acoustic wave propagating in air, especially for a narrow module like this. This is something proved in Section 4.3.2, where a straightangle setup has a smaller phase shift, despite having a larger physical distance between the modules, due to the upwind transceiver in the path of airflow.

A preferable solution would be to find a mechanical setup that ensures that the primary airflow always align with the measurement direction of the sensor, or alternatively, even find a solution for the sensor module that enables a two-dimensional airspeed measurement. However, this indicates that extensive testing and development of the mechanical sensor setup is required before it can operate effectively in a drone application.

6.4 Wet Conditions Impact on Hardware

The transceiver modules in the current configuration may exhibit similar drawbacks as those of the current tube systems used in the drone. The module features an acoustic port leading to a vibrating membrane, which also poses a risk of becoming clogged by water or ice, which could degrade signal quality to various extents.

This is something that has to be investigated and evaluated further, as there is currently limited available data regarding the effect of moisture exposure on this type of system. The CH-101 modules already incorporates a particle ingress filter [37]. However, this is only intended to protect the electronics from particles and liquids, not the acoustic port. Nevertheless, the manufacturer recommends caution in environments including particles and moisture, where protective solutions for dust has been proposed. No equivalent solution has been proposed for moisture protection of the port. However, one suggestion could be to investigate protective membranes or acoustic shielding used in other audio-related applications, although it would require extensive testing and evaluation.

6.5 Ethical Considerations

The military was the reason why drones were developed in the first place, and the first fixed-wing drones were developed during world war one, due to the possibility to perform dangerous missions without risking the lives of pilots [39]. The military applications have dominated the market ever since, and during the last few years the military has maintained a market share reported around 50% [40] up to over 60% [41]. When trying to contribute to the development of vehicles like drones, it will therefore always be a risk contributing to the development of military equipment and the ethical and societal concerns related to this topic. However, the purpose of this project is to develop equipment that can support the Swedish Sea Rescue Society in their missions, and has no intentions to contribute to the military.

Further, the growing use and development of drones for civilian airspace has raised concerns about safety and security, where small mistakes can cause dangerous situations for humans and damage to property [42]. When developing a device that is crucial for the reliability and airworthiness of a drone, it is therefore important to make sure that the device is properly tested before it is integrated. This project did not plan to reach the state of drone integration, but it is still important to reflect on this, and convey potential risks.

Generative artificial intelligence was used during this project to clarify unclear documentation and explain general technical concepts. It was also used to support the writing process by suggesting ways to improve the clarity and wording of the text. However, all design decisions and system development were carried out independently by the author. The author also takes full responsibility for the final wording and content of this report.

7 Conclusion

This thesis has explored the feasibility of utilizing ultrasonic MEMS to develop an ultrasonic airspeed sensor for lightweight fixed-wing drones. The project demonstrates a prototype that offers advantages in terms of size, weight and power consumption, with the potential to match conventional Pitot-static systems. This indicates that the prototype has approached the primary purpose of this project: to reach a smaller sensor design, better suited for these types of applications.

The developed prototype is able to accurately record airspeeds ranging from 0 m/s to 25 m/s in one direction. It is also able to handle rapid changes in airflow with a relatively high responsiveness. However, further testing and development will be needed before it can operate in a real drone application, with rapid changes in airflow and shifting weather conditions. There are also inherent challenges and limitations associated with the pitch and catch technique itself, where the main issue lies in how sound propagates through the air between the transceiver modules. This places significant demands on the mechanical design, as the sensor is not able to rely on robust and large rigs in such applications.

In conclusion, this thesis demonstrates both strengths and limitations of this type of hardware, as well as the ultrasonic airspeed measurement technique in general. However, there are many different techniques available for measuring airspeed, but if ultrasonic sensing is chosen for further development, then the MEMS-based transceiver modules are strong candidates for implementation.

Bibliography

[1] W. Gracey, "Measurement of aircraft speed and altitude," NASA Langely Research Center, Hampton, VA, Tech. Rep. NASA-RP-1046, May 1980, Accessed on: Dec. 05, 2025. [Online]. Available: https://ntrs.nasa.gov/api/citations/19800015804/downloads/19800015804.pdf

[2] Sjöräddningssällskapet, "sjoraddning.se," https://www.sjoraddning.se/, Accessed: Dec. 01, 2025.

[3] H. Male, "An ultrasonic airspeed sensor prototype for a fixed-wing drone," Master's thesis, Chalmers University of Technology, 2023.

[4] J. Geraghty, "An ultrasonic anemometer for lightweight fixed-wing uav airspeed measurements," Master's thesis, Chalmers University of Technology, 2025.

[5] E. Arens, A. Ghahramani, R. Przybyla, M. Andersen, S. Min, T. Peffer, P. Raftery, M. Zhu, V. Luu, and H. Zhang, "Measuring 3d indoor air velocity via an inexpensive low-power ultrasonic anemometer," *Energy and Buildings*, vol. 211, p. 109805, 03 2020.

[6] University of Manchester, "Sonic anemometers," https://www.cas.manchester.ac.uk/restools/instruments/meteorology/sonic/, Accessed on: Dec. 02, 2025.

[7] A. Ghahramani, M. Zhu, R. J. Przybyla, M. P. Andersen, P. J. Galicia, T. E. Peffer, H. Zhang, and E. Arens, "Measuring Air Speed With a Low-Power MEMS Ultrasonic Anemometer via Adaptive Phase Tracking," *IEEE Sensors Journal*, vol. 19, no. 18, pp. 8136–8145, 2019.

[8] *Ultra-low Power Integrated Ultrasonic Time-of-Flight Range Sensor*, TDK Invensense, Dec 2020, Accessed on: Jan. 19, 2026. [Online]. Available: https://invensense.tdk.com/wp-content/uploads/2022/04/DS-000331-CH101-v1.4.pdf

[9] *DLVR Low Voltage Digital Pressure Sensor Series*, ALL SENSORS, Rev. DS-0300, Accessed on: Jan. 29, 2026. [Online]. Available: https://428059.fs1.hubspotusercontent-na1.net/hubfs/428059/Product-Data-Sheets/DS-0300.pdf

[10] M. Toa and A. Whitehead, "Ultrasonic Sensing Basics," Texas Instruments, Dec. 2021, revision D, Accessed on: 2026-02-09.

[11] D. A. Bohn, "Environmental effects on the speed of sound," *Journal of The Audio Engineering Society*, vol. 36, pp. 223–231, 1988.

[12] H. Dong and Y. Jun, "High accuracy time of flight measurement for ultrasonic anemometer applications," in *2013 Third International Conference on Instru-*

mentation, Measurement, Computer, Communication and Control, 2013, pp. 61–64.

[13] D. Han, S. Kim, and S. Park, "Two-dimensional ultrasonic anemometer using the directivity angle of an ultrasonic sensor," *Microelectronics Journal*, vol. 39, no. 10, pp. 1195–1199, 2008. [Online]. Available: https://www.sciencedirect.com/science/article/pii/S002626920800116X

[14] C. Yu, C. Guo, J.-y. Liang, and T. Wang, "Ultrasonic wind velocity measurement based on phase discrimination technique," *TELKOMNIKA Indonesian Journal of Electrical Engineering*, vol. 10, 10 2012.

[15] K. Maenaka, "Current MEMS technology and MEMS sensors -focusing on inertial sensors-," in *2008 9th International Conference on Solid-State and Integrated-Circuit Technology*, 2008, pp. 2371–2374.

[16] W. Gong, X. Wang, Z. Yang, Z. Zhai, W. Feng, and D. Liu, "Ultrasonic thickness measurement method and system implementation based on sampling reconstruction and phase feature extraction," *Sensors*, vol. 23, no. 22, 2023. [Online]. Available: https://www.mdpi.com/1424-8220/23/22/9072

[17] P. Tipler and G. Mosca, *"Chapter 15: Traveling Waves" in Physics for Scientists and Engineers*, ser. Physics for Scientists and Engineers. W. H. Freeman, 2007, no. 133.

[18] S. Smith, *"Chapter 14: Introduction to digital filters" in The Scientist and Engineer's Guide to Digital Signal Processing.* San Diego, CA: California Technical Pub., 1999.

[19] T. C. Singh and M. Kumar, "Digital FIR Filter Designs," in *2021 Asian Conference on Innovation in Technology (ASIANCON)*, 2021, pp. 1–5.

[20] S. Smith, *"Chapter 19: Recursive Filters" in The Scientist and Engineer's Guide to Digital Signal Processing.* San Diego, CA: California Technical Pub., 1999.

[21] *NI-RFSG User Manual*, National Instruments, 2026, Accessed on: 2026-03-23. [Online]. Available: https://www.ni.com/docs/en-US/bundle/ni-rfsg/page/user-manual-welcome.html?srsltid=AfmBOoqDL4d4es4P-W1WNe2V2M3NrZvpweAaIwCvHqL-8a4v4T2Omzjp

[22] "Understanding quadrature demodulation," All About Circuits, Accessed on: 2026-03-22. [Online]. Available: https://www.allaboutcircuits.com/textbook/radio-frequency-analysis-design/radio-frequency-demodulation/understanding-i-q-signals-and-quadrature-modulation/

[23] KiCad, "KiCad," Accessed on: 2026-03-31. [Online]. Available: https://www.kicad.org/

[24] Autodesk, "Autodesk Fusion," Accessed on: 2026-03-30. [Online]. Available: https://www.autodesk.com/products/fusion-360/overview

[25] Prusa Research, "PrusaSlicer 2.9.4," Accessed on: 2026-03-30. [Online]. Available: https://www.prusa3d.com/page/prusaslicer_424/

[26] ——, "Original Prusa MK4S 3D Printer ," Accessed on: 2026-03-30. [Online]. Available: https://www.prusa3d.com/product/original-prusa-mk4s-3d-printer/

[27] Raspberry Pi Ltd, "RP2040 Datasheet ," raspberrypi.com, Accessed on: 2026-04-03. [Online]. Available: https://pip-assets.raspberrypi.com/categories/814-rp2040/documents/RP-008371-DS-1-rp2040-datasheet.pdf?disposition=inline

[28] Visual Studio Code, "C/C++ for Visual Studio Code," code.visualstudio.com, Accessed on: 2026-03-30. [Online]. Available: https://code.visualstudio.com/docs/languages/cpp

[29] Raspberry Pi Ltd, "Get started with Raspberry Pi Pico-series and VS Code," Accessed on: 2026-03-30. [Online]. Available: https://www.raspberrypi.com/news/get-started-with-raspberry-pi-pico-series-and-vs-code/

[30] TDK Invensense, "SonicLib," Accessed on: 2026-03-30. [Online]. Available: https://github.com/tdk-invn-oss/ultrasonic.soniclib

[31] *SonicLib Programmer's Guide for SonicLib v4*, TDK InvenSense, 2024, Revision: 3.0Accessed on: 2026-03-30. [Online]. Available: https://d17t6iyxenbwp1.cloudfront.net/s3fs-public/2026-03/an-000175-chirp-microsystems-soniclib-programmers-guide.pdf?VersionId=ZM6kbp4oUAfxcBK.Sw_vHxYJHt0YvHG2

[32] MathWorks, "Matlab," Accessed on: 2026-03-31. [Online]. Available: https://se.mathworks.com/products/matlab.html

[33] ——, "Signal processing toolbox," Accessed on: 2026-03-31. [Online]. Available: https://se.mathworks.com/products/signal.html

[34] *EV_MOD_CH101 Evaluation Module User Guide*, TDK InvenSense, 2020, Revision: 1.0 Accessed on: 2026-04-05. [Online]. Available: https://product.tdk.com/system/files/dam/doc/product/sensor/ultrasonic/tof/app_note/an-000231-ev_mod_ch101-evaluation-module-user-guide.pdf

[35] B. S. Lee, "Understanding the Terms and Definitions of LDO Voltage Regulators," Texas Instruments, Oct. 1999, SLVA079 Accessed on: 2026-04-04.

[36] *MCP1702-250 mA Low Quiescent Current LDO Regulator*, MICROCHIP, 2010, Accessed on: 2026-04-04. [Online]. Available: https://ww1.microchip.com/downloads/en/devicedoc/22008e.pdf

[37] *CH101 Design Guide*, TDK InvenSense, 2022, Revision: 1.2 Accessed on: 2026-04-05. [Online]. Available: https://d17t6iyxenbwp1.cloudfront.net/s3fs-public/2026-03/an-000259-ch101-design-guide.pdf?VersionId=m3MSidE7Pi0HFqxS6ej.sigUtkkJgTLq

[38] 3DR Inc, "3DR CAN Airspeed Sensor DLVR - M10090," https://docs.3dr.com/dronecan/airspeed-dlvr/, Accessed on: 2026-05-19.

[39] M. Dr. Palik and M. Nagy, "Brief History of UAV Development," *Repüléstudományi Közlemények (Aeronautical Science Bulletins)*, vol. 31, pp. 155–166, 05 2019.

[40] "Global drone market size, share analysis report by type (fixed-wing drone, rotary wing drone), by application (consumer, commercial (construction,

agriculture, oil and gas, mining, public safety and law enforcement, others), military), by region and companies - industry segment outlook, market assessment, competition scenario, trends, and forecast 2025-2034," https://market.us/report/drone-market/, market.us, Accesed on: Jan. 20, 2026.

[41] "UAV Drones market Size, Share, Growth, and Industry Analysis, By Type (Fixed Wing, Rotating Wing, Hybrid), By Application (Military UAV, Civilian UAV), Regional Insights and Forecast to 2034," https://www.marketreportsworld.com/market-reports/uav-drones-market-14722242, Market Reports World, Accesed on: Jan. 20, 2026.

[42] B. Rao, A. G. Gopi, and R. Maione, "The societal impact of commercial drones," *Technology in Society*, vol. 45, pp. 83–90, 05 2016.